

# Quantum speed limit for complex dynamics

Mao Zhang, Huai-Ming Yu, and Jing Liu<sup>✉\*</sup>

National Precise Gravity Measurement Facility, MOE Key Laboratory of Fundamental Physical Quantities Measurement, School of Physics, Huazhong University of Science and Technology, Wuhan 430074, China

Quantum speed limit focuses on the minimum time scale for a fixed mission and hence is important in quantum information where fast dynamics is usually beneficial. Most existing tools for the depiction of quantum speed limit are the lower-bound-type tools, which are in fact difficult to reveal the true minimum time, especially for many-body systems or complex dynamics. Therefore, the evaluation of this true minimum time in these scenarios is still an unsolved problem. Hereby we propose a three-step (classification-regression-calibration) methodology based on machine learning to evaluate the true minimum time in complex dynamics. Moreover, the analytical expression of the true minimum time is also provided for the time-dependent Hamiltonians with time-independent eigenstates.

Quantum speed limit (QSL) is a fundamental topic in quantum mechanics focusing on the characterization of minimum time for quantum states to fulfill certain known targets, such as rotating a state to its orthogonal states, or some angles quantified by certain metrics. In principle, the target could be chosen flexibly due to the problem of interest. In the year of 1945, Mandelstam and Tamm provided the first lower bound for this minimum time based on the uncertainty relation [1]. In 1996 Braunstein *et al.* extended the lower bound to time-dependent Hamiltonians utilizing the generalized uncertainty relation [2] where the time-average variance was applied. In 1998, Margolus and Levitin [3] provided another bound based on the mean energy. After these pioneer works, the topic of QSL entered a period of rapid development in the next 20 years, especially in 2010s [4–42].

Most existing tools in QSL belong to the lower-bound-type (LBT) tools. The advantage of this type of tools is that they are easy to compute, especially in numerical aspects. However, the disadvantage of them are also significant. On one hand, most LBT tools are dependent on the initial states. This dependence would cause a problem that even the initial state cannot actually fulfill the given target, the LBT tools would still provide finite results, which is reasonable in mathematics since any finite value is a legitimate lower bound of infinity. However, it also indicates that from these tools one cannot acquire the information whether a state is capable to fulfill the target. For example, consider a qubit Hamiltonian  $\omega\sigma_z/2$  with  $\sigma_{z(x)}$  the Pauli Z (X) matrix and  $\omega$  the energy gap. For this Hamiltonian, the Mandelstam-Tamm and Margolus-Levitin bounds for the state with the density matrix  $\mathbb{1}/2 + \sigma_x/4 + \sqrt{3}\sigma_z/4$  are  $2\pi/\omega$  and  $2\pi/(\sqrt{3}\omega)$ . Here  $\mathbb{1}$  is the identity matrix. However, in fact this state cannot fulfill the target  $\pi/2$  at all since the maximum angle it can rotate under the given Hamiltonian is only  $\pi/3$  [21]. Hence, without the information whether the target can be fulfilled, the conclusions based on the lower-bound-type tools might be suboptimal since

the results are actually unphysical for the states unable to reach the target.

On the other hand, in the case that the Hamiltonians are time-dependent, the LBT tools are usually functions of time [9–20]. As a matter of fact, these formal time-dependent lower bounds are difficult to reveal both the true minimum time and true physics behind it. As clarified in Ref. [21], in noncontrolled scenarios the true minimum time for a fixed state to fulfill a given target is only a fixed time point, and the results of LBT tools have to go across this time point due to their time dependence. During the time before this time point, the finite results of the LBT tools cannot reveal the fact that this state is actually incapable to reach the target in the time regime. And during the time after this time point, the results of LBT tools have to be no larger than this point since they are its lower bounds, which indicates that in this time regime the attainability of the LBT tools is lousy. These disadvantages of LBT tools could be further magnified with the growth of system dimension or the complexity of dynamics. Hence, locating the true minimum time for the fulfillment of a given target in many-body systems and complex dynamics is still an important yet unsolved problem. Finding this minimum time or at least providing efficient methodologies to search it is thus the major motivation of this paper.

## Results and discussion

### Operational definition of the quantum speed limit

The target in QSL could be quantified via different tools, such as the Bures metric or various types of fidelity [8–13], relative purity [14–16], Bloch angle [16, 17, 21, 22], gauge invariant distances [18, 19], and Wigner-Yanase information [20]. Different tools usually lead to different mathematical bounds or methods for the description of QSL, and a general and unified methodology that fits all tools is still in lack. Recently, an operational definition of the quantum speed limit (OQSL) was proposed [21] based on the Bloch angle, which is capable to be extended to a general tool due to the fact that it is intrinsically a methodology, rather than a concept. Denote  $\rho$  as the density matrix of a quantum state,  $\Phi$

\* liujingphys@hust.edu.cn

as any type of metric or tool to quantify the target and  $\Phi_{\text{tar}}$  as the corresponding target value, then the reachable state set can be defined as  $\mathcal{S} := \{\rho | \Phi(t, \rho) = \Phi_{\text{tar}}, \exists t\}$ , which is the set of states that can fulfill the target. Moreover, it is possible that in some cases not all states in the state space, but the states in a subset  $\mathcal{Q}$ , are concerned. In this case,  $\mathcal{S}$  can be further expressed by  $\mathcal{S} := \{\rho | \rho \in \mathcal{Q} \ \& \ \Phi(t, \rho) = \Phi_{\text{tar}}, \exists t\}$ . Utilizing  $\mathcal{S}$ , the OQSL (denoted by  $\tau$ ) can be defined by

$$\tau := \min_{\rho \in \mathcal{S}} t \quad \text{subject to } \Phi(t, \rho) = \Phi_{\text{tar}}. \quad (1)$$

The Bloch vector is one of the most famous geometric representations for the quantum state and has been widely applied in many fields of quantum physics, such as the quantum computation [43] and quantum control [44]. In the Bloch representation, the density matrix can be expressed by  $\rho = \frac{1}{N}(\mathbb{1} + \sqrt{\frac{1}{2}N(N-1)}\vec{r} \cdot \vec{\lambda})$ , where  $N$  is the dimension of  $\rho$ ,  $\vec{\lambda}$  is the vector of  $SU(N)$  generators,  $\vec{r}$  is the Bloch vector satisfying  $|\vec{r}| \leq 1$ , and  $\mathbb{1}$  is the identity matrix. The Bloch angle  $\theta$  between  $\vec{r}$  and its evolved vector  $\vec{r}(t)$  is  $\theta(t, \vec{r}) := \arccos\left(\frac{\vec{r} \cdot \vec{r}(t)}{|\vec{r}||\vec{r}(t)|}\right) \in (0, \pi]$ . Denote  $\Theta$  as the fixed target, then the reachable state set can be rewritten into  $\mathcal{S} = \{\vec{r} | \vec{r} \in \mathcal{Q} \ \& \ \theta(t, \vec{r}) = \Theta, \exists t\}$ , and the OQSL reads  $\tau = \min_{\vec{r} \in \mathcal{S}} t$ , subjecting to the constraint  $\theta(t, \vec{r}) = \Theta$ .

In the perspective of OQSL, when two tools to quantify the target has a one-to-one correspondence, for example the angle of relative purity  $\arccos\left(\frac{\text{Tr}(\rho\rho(t))}{\text{Tr}(\rho^2)}\right)$  and Bloch angle (calculation details are in the Supplementary Information), then the reachable state sets for these tools are exactly the same, which means the results of OQSL would also be equivalent. This equivalence reveals an important fact that a physical target can be mathematically quantified by different tools, yet the true minimum time to fulfill the physical target should not be affected by this quantification process since it is not physical.

The OQSL is closely related to the quantum brachistochrone problem [45, 46], which focuses on searching the minimum time for a given initial state to a fixed target state or the realization of a target gate. In the language of OQSL, instead of a given initial state, we can study the minimum time for a set of initial states, i.e., the aforementioned set  $\mathcal{Q}$ , to reach a target state  $\rho_{\text{tar}}$  under a given Hamiltonian. In this problem  $\mathcal{S}$  can be expressed by  $\mathcal{S} = \{\rho | \rho \in \mathcal{Q} \ \& \ e^{\mathcal{L}}(\rho) = \rho_{\text{tar}}, \exists t\}$  where  $\mathcal{L}$  is a superoperator satisfying  $\partial_t \rho_t = \mathcal{L}(\rho_t)$  with  $\rho_t$  the evolved state of  $\rho$ . Furthermore, the OQSL can be expressed by

$$\tau := \min_{\rho \in \mathcal{S}} t \quad \text{subject to } e^{\mathcal{L}}(\rho) = \rho_{\text{tar}}. \quad (2)$$

Notice that if  $\rho_{\text{tar}} \in \mathcal{Q}$ , the optimal state in  $\mathcal{Q}$  to reach  $\rho_{\text{tar}}$  must be  $\rho_{\text{tar}}$  itself for any Hamiltonian and the corresponding time is nothing but zero, which means

this is a trivial case. Therefore,  $\rho_{\text{tar}} \notin \mathcal{Q}$  should be satisfied to make sure the problem is nontrivial. Here we still take the qubit Hamiltonian  $\omega\sigma_z/2$  as a simple demonstration. The target state is assumed to be  $(|0\rangle - |1\rangle)/\sqrt{2}$  with  $|0\rangle$  ( $|1\rangle$ ) the eigenstate of  $\sigma_z$  corresponding to the eigenvalue 1 ( $-1$ ).  $\mathcal{Q} = \{\rho | \text{Tr}(\rho\sigma_x) \geq 0\}$ . Utilizing the spherical coordinates of the Bloch vector  $\vec{r} = \eta(\sin\alpha\cos\varphi, \sin\alpha\sin\varphi, \cos\alpha)^T$ ,  $\mathcal{S}$  in this example reads  $\{\vec{r} | \eta = 1, \alpha = \pi/2, \varphi \in [0, \pi/2] \cup [3\pi/2, 2\pi)\}$ , and the OQSL  $\tau = \pi/(2\omega)$ . This minimum time can be attained by the state  $(|0\rangle + i|1\rangle)/\sqrt{2}$ . Calculation details can be found in the Supplementary Information.

Compared to lower-bound-type QSLs, the advantages of OQSL are that it can reveal the information that whether a state can fulfill the target, and it is always attainable [21]. In the case of complex dynamics, these advantages come at a price of high computational complexity, which is not only due to the optimization in the definition, but also the preliminary assumption that  $\mathcal{S}$  is known. For example, in the analytical calculation of the OQSL, the search of  $\mathcal{S}$  is the first step and usually finished by finding the condition of  $\rho$  when the equation  $\Phi(t, \rho) = \Phi_{\text{tar}}$  has a finite solution  $t$ . Then the evolution time to fulfill the target is calculated and optimized under this condition to further obtain the OQSL. In this case, the calculation of  $\mathcal{S}$  and the optimization of time are performed separably and thus their contributions to the computational complexity are different. In the numerical evaluation of OQSL, the contributions of these two processes are the same when the brute-force search is applied since the search of  $\mathcal{S}$  in this method is based on the rigorous dynamics of each state. When  $\mathcal{S}$  is obtained, the corresponding time to fulfill the target for each state is also obtained. Hence, the computational complexity in this case is basically contributed by the search of  $\mathcal{S}$ . However, it is obvious that the brute-force search is not always feasible in practice, especially when the dynamics is complex or the system size is large, which is actually a non-negligible scenario in the study of QSL [23–26]. Hence, finding methods for the evaluation of OQSL that are friendly to the complex dynamics or large-size systems is critical, and thus the major motivation of this paper.

### The time-dependent Hamiltonians with time-independent eigenstates

In many cases, the complexity of dynamics comes from the time dependency of the Hamiltonian. The OQSL for a general time-dependent Hamiltonian is difficult to obtain analytically. However, for the time-dependent Hamiltonians with time-independent eigenstates, the OQSL can be obtained analytically when taking the Bloch angle as the quantification of target. In the energy space, these Hamiltonians can be expressed by  $H(t) = \sum_i E_i(t) |E_i\rangle \langle E_i|$ , where the eigenstate  $|E_i\rangle$  is time-independent for any  $i$  and the eigenvalue  $E_i(t)$  depends on time. Many well-known models in quantum mechanics fit this scenario, such as the one-dimensional

Ising model with a time-varying longitudinal field, the resonant Jaynes-Cummings model with time-dependent coupling [47–49], and the semiclassical qubit-field model in the strong coupling regime [50]. For such Hamiltonians, we present the following theorem.

**Theorem.** For a  $N$ -dimensional time-dependent Hamiltonian whose eigenstates are all time-independent, the OQSL  $\tau$  satisfies the equation

$$\int_0^\tau [E_{\max}(t) - E_{\min}(t)] dt = \Theta, \quad (3)$$

where  $E_{\max}(t)$  and  $E_{\min}(t)$  are the maximum and minimum energies of the Hamiltonian at time  $t$ . Further denoting the  $p$ -dimensional set  $\{|E_{\min}\rangle\}$  and  $q$ -dimensional set  $\{|E_{\max}\rangle\}$  as the sets of eigenstates with respect to  $E_{\min}(t)$  and  $E_{\max}(t)$ , the optimal states to reach the OQSL are

$$\sum_i \frac{1}{N} |E_i\rangle \langle E_i| + \sum_{\substack{|E_k\rangle \in \{|E_{\min}\rangle\}, \\ |E_l\rangle \in \{|E_{\max}\rangle\}}} \xi_{kl} |E_k\rangle \langle E_l| + \xi_{kl}^* |E_l\rangle \langle E_k|,$$

where the matrix  $\xi$  (with  $kl$ th entry  $\xi_{kl}$ ) satisfies  $N^2 \xi^\dagger \xi \leq \mathbb{1}_q$  with  $\mathbb{1}_q$  the  $q$ -dimensional identity matrix.

The proof is given in the Supplementary Information. As a matter of fact, this theorem covers Theorem 1 in Ref. [21] due to the fact that Eq. (3) reduces to  $\tau = \Theta/(E_{\max} - E_{\min})$  when the eigenvalues are time-independent. As a simple demonstration, consider the Hamiltonian  $H(t) = f(t)\sigma_z$  with  $f(t)$  a time-dependent function. It is obvious that the eigenstates of this Hamiltonian are independent of time. Hence the corresponding OQSL is given in the theorem above. In the case that  $|\int_0^\tau f(t_1) dt_1|$  is upper bounded by  $c_f$ ,  $\mathcal{S}$  is fully determined by the value of  $c_f$ , which leads to the following corollary.

**Corollary.** For the Hamiltonian  $H(t) = f(t)\sigma_z$  where  $f(t)$  satisfies  $|\int_0^\tau f(t_1) dt_1| \leq c_f$ , no state can fulfill the target  $\Theta$  if  $c_f < \Theta/2$ .

In the case that  $c_f \geq \Theta/2$ ,  $\mathcal{S}$  is symmetric about  $z$  axis in the Bloch sphere, similar to the time-independent Hamiltonian  $\omega\sigma_z/2$  [21]. This is due to the fact that in this case the dynamics of all states in the Bloch sphere are the precessions about  $z$  axis, and thus it obeys the rotational symmetry about  $z$  axis. Therefore,  $\mathcal{S}$  can be fully expressed by the angle between the Bloch vector and  $z$  axis (denoted by  $\alpha$ ). More specifically to say, when  $c_f \in [\Theta/2, \pi/2]$ ,  $\mathcal{S} = \{\vec{r} | \alpha \in [\alpha_f, \pi - \alpha_f]\}$  with  $\alpha_f = \arcsin\left(\frac{\sin(\Theta/2)}{\sin c_f}\right)$ , and  $\mathcal{S} = \{\vec{r} | \alpha \in [\Theta/2, \pi - \Theta/2]\}$  when  $c_f > \pi/2$ . Furthermore, the OQSL satisfies  $\int_0^\tau |f(t)| dt = \Theta/2$ . A physical example here is  $f(t) = -g\mu_B B \cos(\omega t)/2$  [51] with  $g$  the Lande factor,  $\mu_B$  the electron magnetic moment and  $B \cos(\omega t)$  a periodic magnetic field. Due to the fact  $|\int_0^\tau f(t_1) dt_1| \leq g\mu_B B/(2\omega)$ ,  $\mathcal{S}$  is determined by the ratio between  $B$  and  $\omega$ . The OQSL reads  $\tau = \arcsin\left(\frac{\omega\Theta}{g\mu_B B}\right)/\omega$ , and

the optimal states are the states in the  $xy$  plane. It is obvious that  $\tau \leq \pi/(2\omega)$  as  $\arcsin(\cdot)$  is always less than or equal to  $\pi/2$ . This upper bound is nothing but the time when the first degenerate point occurs, which leads to an interesting phenomenon that *all targets can be fulfilled before the first degenerate point occurs* with the states in the  $xy$  plane. In the case that a bounded control  $u(t)$  ( $|u(t)| \leq u_b$ ) is invoked,  $f(t)$  becomes  $u(t) - g\mu_B B \cos(\omega t)/2$  and the upper bound of  $|\int_0^\tau f(t_1) dt_1|$  can always overcome  $\pi/2$  at a long enough time. Hence, in this case  $\mathcal{S} = \{\vec{r} | \alpha \in [\Theta/2, \pi - \Theta/2]\}$  and the OQSL satisfies  $\int_0^\tau |g\mu_B B \cos(\omega t)/2 - u(t)| dt = \Theta/2$ . The minimum  $\tau$  with respect to  $u(t)$  (denoted by  $\tau_{\min}$ ) satisfies the equation  $g\mu_B B \sin(\omega\tau_{\min})/(2\omega) + u_b\tau_{\min} = \Theta/2$ , and  $\tau_{\min} \approx \Theta/(g\mu_B B + 2u_b)$  for a small  $\omega$ . The calculation details are in the Supplementary Information.

Another practical scenario to apply Theorem 1 is the one-dimensional Ising model with a longitudinal field, where two boundary conditions (periodic and open) exist. Let us first consider the case of periodic boundary condition, in which the Hamiltonian reads  $H/J = -\sum_{j=1}^n \sigma_j^z \sigma_{j+1}^z - \sum_{j=1}^n g(t) \sigma_j^z$  with  $\sigma_{n+1}^z = \sigma_1^z$ . Here  $J > 0$  is the interaction strength of the nearest-neighbor coupling, and  $g(t)$  is a global time-dependent longitudinal field.  $\sigma_j^z$  is the Pauli Z matrix for  $j$ th spin. The spin number  $n \geq 3$ . In this case, the minimum energy is  $-n[1+|g(t)|]$ , and the maximum energy is  $n - \eta[2-|g(t)|]$  when  $|g(t)| < 2$  and  $n[|g(t)| - 1]$  when  $|g(t)| \geq 2$ . Here  $\eta := [1 + (-1)^{n+1}]/2$ . If  $|g(t)| \geq 2$  for all time  $t$ , the OQSL satisfies the equation  $\int_0^\tau |g(t)| dt = \Theta/(2n)$ . Due to the fact that  $\int_0^\tau |g(t)| dt \geq \int_0^\tau 2 dt = 2\tau$ , one can immediately find that  $\tau \leq \Theta/(4n)$ . If  $|g(t)| < 2$  all the time, Eq. (3) reduces to  $2(n - \eta)\tau + (n + \eta)\int_0^\tau |g(t)| dt = \Theta$ . In this case  $\tau \in [\frac{\Theta}{4n}, \frac{\Theta}{2n-2\eta}]$  since  $\int_0^\tau |g(t)| dt \in [0, 2\tau]$ . For a  $g(t)$  that is not always bounded by 2, the integration in Eq. (3) needs to be calculated part by part and the rigorous solution may not easy to be acquired in general. However, in some cases a good approximation can still be obtained since  $\tau$  is usually small. Take  $g(t) = B \cos(\omega t)$  as an example, where  $B$  and  $\omega$  are the amplitude and frequency. In this case, if  $\omega$  is not very large, then  $\tau \approx \Theta/[2(n - \eta) + B(n + \eta)]$  when  $B < 2$  and  $\tau \approx \Theta/(2Bn)$  when  $B \geq 2$ , which are nothing but the OQSLs with respect to the constant field  $g(t) = B$ .

In the case of open boundary condition, the Hamiltonian reads  $-\sum_{j=1}^{n-1} \sigma_j^z \sigma_{j+1}^z - \sum_{j=1}^n g(t) \sigma_j^z$ . The minimum energy is  $-n[1+|g(t)|] + 1$ , and the maximum energy is  $n + \eta|g(t)| - 1$  when  $|g(t)| \leq 1$ ,  $n - (2 - \eta)[2 - |g(t)|] + 1$  when  $|g(t)| \in (1, 2)$ , and  $n[|g(t)| - 1] + 1$  when  $|g(t)| \geq 2$ . For  $g(t) = B \cos(\omega t)$  with a not very large  $\omega$ , an interesting phenomenon occurs when  $B < 2$  and  $n$  is even. The OQSL in this case approximates to  $\Theta/[n(B+2)-2]$  when  $B \leq 1$ , and  $\Theta/[n(B+2) + 2(B-2)]$  when  $B \in (1, 2)$ , which are different from the OQSL under the periodic boundary condition. These two OQSLs, as well as their difference, are quite robust to global and local dephasing. Therefore, the OQSL may be used to detect whether an

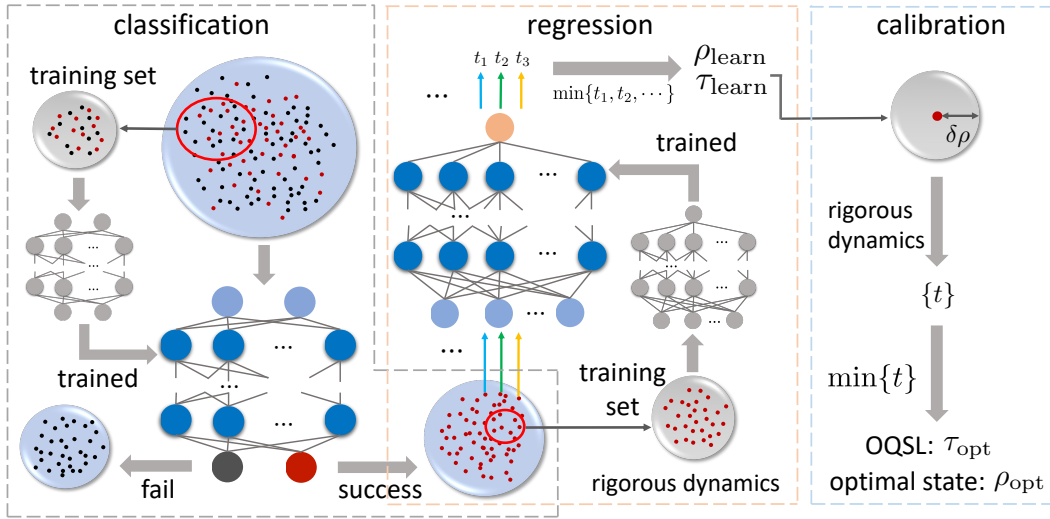


Figure 1. CRC methodology to learn the OQSL for complex dynamics. The three steps are classification (gray box), regression (orange box), and calibration (blue box).

even-numbered spin ring is ruptured, especially when the number is not very large. More details are in the Supplementary Information.

### CRC methodology

The brute-force search is the most common method for the numerical evaluation of OQSL and is easy to execute for simple dynamics. However, when the evaluation of dynamics for one state is too time-consuming, the entire brute-force search would be impossible to finish as it usually requires executing thousand and even million rounds of dynamics. In recent years, machine learning has been successfully applied to quantum physics for the simulation of complex dynamics, such as the theoretical dynamics of many-body systems [52–54] and realistic dynamics of experimental systems [55, 56]. With the help of trained neural networks, the computing time to evaluate the dynamics significantly reduces compared to the rigorous calculation. Therefore, such learning techniques could be powerful tools to evaluate the OQSL. Hereby we provide a three-step methodology (CRC methodology) based on learning to evaluate the OQSL for complex dynamics. The three steps are (1) classification; (2) regression; and (3) calibration, as illustrated in Fig. 1. As a matter of fact, classification and regression are two terminologies in supervised learning. Classification is a problem to identify the categories of objects and regression is to predict some values related to the objects.

The reachable state set  $\mathcal{S}$  is crucial in the evaluation of OQSL. It is not only essential for the further calculation of OQSL, but also reveals information that whether a state is capable to fulfill the target. Hence, the first step (classification) in CRC methodology is to find  $\mathcal{S}$ . In this step, a reasonable number of quantum states and corresponding binary labels (0 or 1) consist of the training set. Quantum states and binary labels are the input and

output of the neural network. In our calculation, label 1 (0) represents the state is in (not in)  $\mathcal{S}$ . The performance of the trained network can be tested via a test set. After the training and performance verification, a large number of random states are input into the network to construct  $\mathcal{S}$  according to the outputs. In the following the learned reachable state set in this step is denoted by  $\mathcal{S}_{\text{learn}}$ .

The second step is regression. In this step, a subset of  $\mathcal{S}_{\text{learn}}$  and the corresponding time to reach the target consist of the training set. The time to reach the target is extracted from the rigorous dynamics. Notice that it is possible some states in this subset cannot fulfill the target and need to be removed from the training set since  $\mathcal{S}_{\text{learn}}$  could be slightly different from  $\mathcal{S}$  in practice. After the training and performance verification, all states in  $\mathcal{S}_{\text{learn}}$  will be input into the trained network, and the minimum output ( $\tau_{\text{learn}}$ ) and corresponding states ( $\rho_{\text{learn}}$ ) are extracted. The performance of  $\tau_{\text{learn}}$  relies on the performance of the trained neural network in this process. Usually enlarging the scale of the training set is a possible way to improve the performance of learning. However, in many cases this improvement is not always positively correlated to the scale growth of the training set. In the meantime, choosing an appropriate neural network would also be helpful, yet whether a network is appropriate usually needs to be thoroughly tested case by case. Moreover, large-scale models or quantum machine learning are also possible candidates to further improve the performance of  $\tau_{\text{learn}}$ , and we will continue to investigate this problem in the future.

In principle  $\tau_{\text{learn}}$  could be treated as an approximation of OQSL. However, if the methodology stops here then the accuracy of learned OQSL would be strongly affected by the residuals, namely, the differences between the true and predicted values. In the meantime,  $\rho_{\text{learn}}$  may not be

the actual optimal state in the neighborhood due to the existence of residuals. To further improve the methodology's performance, we introduce the third step: calibration. In this step, a reasonable region around  $\rho_{\text{learn}}$  in the state space is picked, and the dynamics of enough random states in this region are calculated rigorously. Then the minimum time to reach the target in this region ( $\tau_{\text{opt}}$ ) and corresponding state ( $\rho_{\text{opt}}$ ) are picked out.  $\tau_{\text{opt}}$  is the final evaluated value of OQSL in the methodology. Due to the fact that the process of calibration is designed to reduce the influence of residuals, a general principle for a proper region in calibration is that in this region it should clearly show that whether  $\rho_{\text{learn}}$  is a local minimum point.

To verify the validity of CRC methodology, we apply it in the Landau-Zener model where the reachable state set and OQSL have been thoroughly discussed via brute-force search among about one million states [21], and thus the methodology's performance is easy to be tested. The Hamiltonian for the Landau-Zener model is  $H = \Delta\sigma_x + vt\sigma_z$  with  $\Delta$  and  $v$  two time-independent parameters. In the step of classification, three training sets with different numbers of data are used to train the network and about one million states are used as the test set. The scores (correctness of prediction) are no less than 99.59%, 97.83%, and 98.00% for all training sets in the cases of  $\Delta = 0, 1$ , and 2. In the step of regression, the mean square errors of learning are on the scale of  $10^{-5}$  for  $\Delta = 0, 2$ , and no larger than  $1.22 \times 10^{-4}$  for  $\Delta = 1$ . In the last step, the region for calibration is chosen as  $[\alpha_{\text{learn}} - 0.1, \alpha_{\text{learn}} + 0.1]$  and  $[\phi_{\text{learn}} - 0.1, \phi_{\text{learn}} + 0.1]$  where  $\alpha_{\text{learn}}$  and  $\phi_{\text{learn}}$  are the spherical coordinates of  $\rho_{\text{learn}}$ , i.e.,  $\cos(\alpha_{\text{learn}}) = \text{Tr}(\rho_{\text{learn}}\sigma_z)$  and  $\cos(\phi_{\text{learn}}) = \text{Tr}(\rho_{\text{learn}}\sigma_x)/\sin(\alpha_{\text{learn}})$ . The results of calibration show that in this case  $\rho_{\text{learn}}$  is just  $\rho_{\text{opt}}$  for all values of  $\Delta$ , and the corresponding  $\tau_{\text{opt}}$  coincides with the exact OQSL obtained from the brute-force search. The validity of CRC methodology is then verified.

One advantage of CRC methodology is that it can deal with controlled dynamics, where the brute-force-search evaluation is usually difficult to realize due to the complexity of twofold optimizations. In the meantime, CRC methodology can also deal with noisy scenarios where the rigorous dynamics is usually more time-consuming than the unitary counterpart. Let us still consider the Landau-Zener model with the time-varying control Hamiltonian  $\vec{u}(t) \cdot \vec{\sigma}$ . Here  $\vec{u} = (u_x(t), u_y(t), u_z(t))$  is the vector of control amplitudes and  $\vec{\sigma} = (\sigma_x, \sigma_y, \sigma_z)$  is the vector of Pauli matrices. All control amplitudes are assumed to be in the regime  $[-\sqrt{v}, \sqrt{v}]$ . Both the noiseless and noisy scenarios are studied. In the noisy scenario, the dynamics is governed by the master equation  $\partial_t \rho = -i[H, \rho] + \gamma(\sigma_z \rho \sigma_z - \rho)$  with  $\gamma$  the decay rate, which is taken as  $0.5\sqrt{v}$  as a demonstration. In this example, the evaluation of OQSL for  $\Delta = 0$  via brute-force search among one million states on a daily-use computer costs more than 830 days, which reduces to 30 days when the CRC methodology is applied [57]. The result of CRC

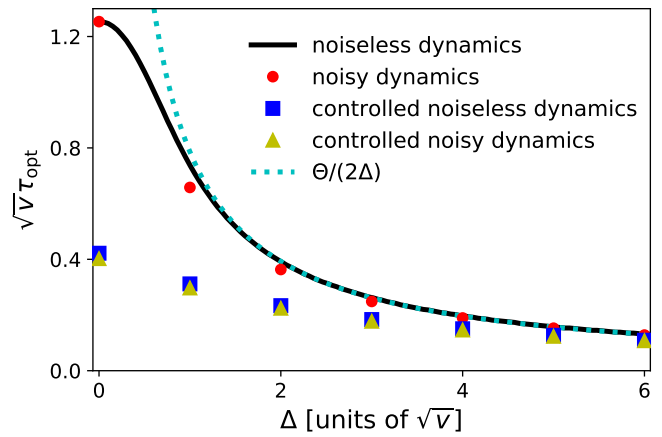


Figure 2. OQSL as a function of  $\Delta$  in the cases of noiseless dynamics (solid black line), noisy dynamics (red circles), controlled noiseless dynamics (blue squares), and controlled noisy dynamics (yellow triangles). The cyan dotted line represents  $\Theta/(2\Delta)$ . The target  $\Theta = \pi/2$ .

methodology shows that all states in the state space can fulfill the target  $\Theta = \pi/2$  under control in both noisy and noiseless cases. Furthermore, the OQSL is very robust to the dephasing in both noncontrolled and controlled cases, as shown in Fig. 2. In the meantime, the controls can significantly reduce the OQSL when  $\Delta$  is not very large. However, this improvement becomes limited with the increase of  $\Delta$ . An interesting phenomenon is that regardless of the existence of both noise and controls, the OQSL always converges to  $\Theta/(2\Delta)$ , which is nothing but the OQSL for the Hamiltonian  $\Delta\sigma_x$  in the absence of noise [21]. This phenomenon on speed limit is difficult to be revealed by lower-bound-type QSLs not only due to their dependence on both initial states and time, but also the lousy attainability when controls are involved.

Another example we studied is the transverse Ising model with a periodic external field. The Hamiltonian is  $H/J = -\sum_{j=1}^n \sigma_j^z \sigma_{j+1}^z - \sum_{j=1}^n g(t) \sigma_j^x$  with  $g(t) = B \cos(\omega t)$ . In the demonstration, the amplitude  $B$  is taken as 0.5 and the frequency  $\omega/J = 1$ . Because of the enormous state space ( $2^n$ ), it is difficult to construct a training set that is general enough for the CRC methodology, especially when  $n$  is large. To feasibly apply the CRC methodology, we need to analyze the state structure first and reduce the state space for the study. A simple way to categorize the states is based on the number of nonzero entries in a certain basis, such as the basis  $\{|\uparrow\rangle, |\downarrow\rangle\}^{\otimes n}$  considered as follows.  $|\uparrow\rangle$  ( $|\downarrow\rangle$ ) is the eigenstate of  $\sigma_z$  with respect to the eigenvalue 1 ( $-1$ ). Moreover, here we only consider the noiseless dynamics and that  $\mathcal{Q}$  is the set of pure states. The ratios of reachable states for the target  $\Theta = \pi/2$  in the categories of 2 (red pentagrams), 3 (green crosses), and 10 nonzero entries (blue triangles) are given in Fig. 3. The ratio in each category is obtained from 2000 random states. It can be seen that basically all states in each category can

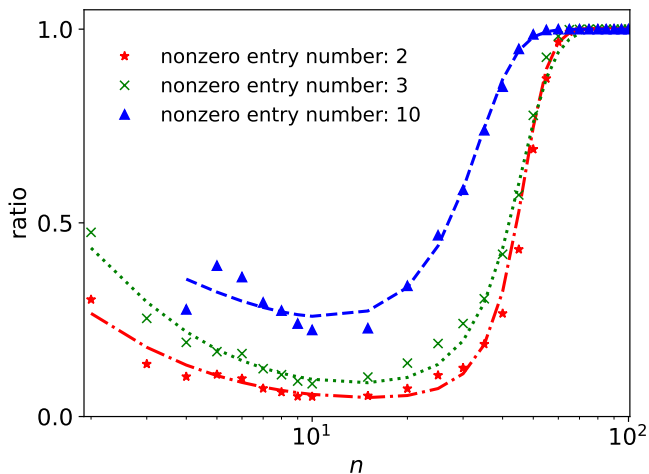


Figure 3. Ratio of states that can fulfill the target  $\Theta = \pi/2$  in different categories. The red pentagrams, green crosses, and blue triangles represent the ratios for the states with 2, 3, and 10 nonzero entries. The dash-dotted red, dotted green, and dashed blue lines represent the corresponding fitting functions.

fulfill the target when  $n$  is large, which is reasonable as more target directions exist when the dimension is high. Moreover, the ratio increases with the rise of the nonzero entry number. More interestingly, the ratio in each category basically fits the function  $1/(1 + an^be^{-cn^d})$ , and the parameters  $a, b, c, d$  can be found in the Supplementary Information. The general behaviors of the ratio and the physical mechanism behind it are still open questions that require further investigation. The minimum time to reach the target for all states in each category is also investigated and the specific results are given in the Supplementary Information, which indicates that in this example we only need to focus on the states with few nonzero entries for the study of OQSL.

Next we perform the CRC methodology in the case of  $n = 10$ . The methodology is applied to the categories of states with 2 to 5 nonzero entries. Here we present the result in the category of 2 nonzero entries, and others are given in the Supplementary Information. 22500 and 7500 states and corresponding labels are used as the training and test sets for the classification. The best score of the trained network we obtained is 94.55%. Then about one million states are input into this network, and the result shows that 7.71% states can fulfill the target, close to the result (5.15%) obtained from 2000 random states. In the regression process, 22500 and 7500 states consist of the training and test sets. The best mean square error is  $8.95 \times 10^{-4}$  and the corresponding  $\tau_{\text{learn}}$  is 0.24, close to the true evolution time (0.19) of  $\rho_{\text{learn}}$ . About 10000 states in the neighborhood of  $\rho_{\text{learn}}$  are used in the calibration and the final result is 0.18. Combing the results of the other three categories, the final value of OQSL obtained from the CRC methodology is 0.18, which can be realized by certain states with 2 nonzero entries.

## Methods

In both cases of controlled Landau-Zener model and transverse Ising model, 22500 and 7500 datasets are generated for training and testing in the classification and regression processes. Each dataset is composed of the initial state and corresponding time to reach the given target. In these datasets, the initial states are generated randomly and the time is solved via rigorous dynamics. In the case of controlled Landau-Zener model, the optimal control is obtained via the automatic differentiation. In the case of transverse Ising model, the initial states are expressed by the matrix product state which is implemented via Julia package ITensors [63], and the time for reaching the given target is calculated with time evolving block decimation technique. In the process of calibration, 10000 datasets are generated in a reasonable neighborhood of  $\rho_{\text{learn}}$ .

The Python package sklearn [61] is used in this paper to build and train the neural networks for the classification and regression processes. In the cases of noncontrolled and controlled Landau-Zener models, the layer number of the neural network is 5 to 6, and each layer contains about 250 neurons. The hyperbolic tangent function and rectified linear unit function are chosen as the activation loss function in the classification and regression, respectively. In the case of transverse Ising model, the neural networks in classification for the states with 2, 3, 4, and 5 nonzero entries are all activated by the hyperbolic tangent function. With respect to the regression, the activation loss function for the neural networks is rectified linear unit function for the states with 2 nonzero entries, logistic function for those with 3 nonzero entries, and identity function for those with 4 and 5 nonzero entries.

In the process of classification, average cross-entropy loss function is used to train the neural networks, which is of the form

$$f(\hat{x}, x, W) = -\frac{1}{m} \sum_{i=0}^m [x_i \ln \hat{x}_i + (1 - x_i) \ln(1 - \hat{x}_i)] + \frac{\alpha}{2m} \|W\|_2^2, \quad (4)$$

where  $x$  and  $\hat{x}$  represent the true results and the results predicted by the neural network.  $m$  is the number of datasets.  $W$  is the weight matrix of the neural network and  $\alpha \|W\|_2^2 = \alpha \sum_{ij} W_{ij}^2$  represents the penalty term. And in the regression, the loss function in the training is the mean square error function,

$$f(t_{\text{pre}}, t_{\text{ext}}, W) = \frac{1}{2m} \sum_{i=0}^m [t_{\text{pre}}^{(i)} - t_{\text{ext}}^{(i)}]^2 + \frac{\alpha}{2m} \|W\|_2^2, \quad (5)$$

here  $t_{\text{pre}}$  and  $t_{\text{ext}}$  are the time predicted by the regression neural network and the exact time obtained via rigorous dynamics. More details of the methods can be found in the Supplementary Information.

When the value of  $\Theta$  is changed, the reachable state set changes accordingly, which means all the neural networks

in the CRC methodology have to be retrained. How to train general neural networks that work for all target values is still a very challenging problem, and requires further and continuous investigations in the future.

## Data availability

The data that support the findings of this study are available from J.L. upon reasonable request.

## Code availability

The code used in this study is available from J.L. upon reasonable request.

- 
- [1] L. Mandelstam and I. Tamm, The uncertainty relation between energy and time in nonrelativistic quantum mechanics, *J. Phys.* **9**, 249 (1945).
- [2] S. L. Braunstein, C. M. Caves, and G. J. Milburn, Generalized Uncertainty Relations: Theory, Examples, and Lorentz Invariance, *Ann. Phys.* **247**, 135 (1996).
- [3] N. Margolus and L. B. Levitin, The maximum speed of dynamical evolution, *Physica D* **120**, 188 (1998).
- [4] V. Giovannetti, S. Lloyd, and L. Maccone, Quantum limits to dynamical evolution, *Phys. Rev. A* **67**, 052109 (2003).
- [5] V. Giovannetti, S. Lloyd, and L. Maccone, The speed limit of quantum unitary evolution, *J. Opt. B* **6**, S807 (2004).
- [6] L. B. Levitin and T. Toffoli, Fundamental Limit on the Rate of Quantum Dynamics: The Unified Bound Is Tight, *Phys. Rev. Lett.* **103**, 160502 (2009).
- [7] T. Caneva, M. Murphy, T. Calarco, R. Fazio, S. Montangero, V. Giovannetti, and G. E. Santoro, Optimal Control at the Quantum Speed Limit, *Phys. Rev. Lett.* **103**, 240501 (2009).
- [8] M. M. Taddei, B. M. Escher, L. Davidovich, and R. L. de Matos Filho, Quantum Speed Limit for Physical Processes, *Phys. Rev. Lett.* **110**, 050402 (2013).
- [9] S. Deffner and E. Lutz, Quantum Speed Limit for Non-Markovian Dynamics, *Phys. Rev. Lett.* **111**, 010402 (2013).
- [10] Z. Sun, J. Liu, J. Ma, and X. Wang, Quantum speed limit for Non-Markovian dynamics without rotating-wave approximation, *Sci. Rep.* **5**, 8444 (2015).
- [11] I. Marvian and D. A. Lidar, Quantum Speed Limits for Leakage and Decoherence, *Phys. Rev. Lett.* **115**, 210402 (2015).
- [12] K. Funo, J.-N. Zhang, C. Chatou, K. Kim, M. Ueda, and A. del Campo, Universal Work Fluctuations During Shortcuts to Adiabaticity by Counterdiabatic Driving, *Phys. Rev. Lett.* **118**, 100602 (2017).
- [13] B. Shanahan, A. Chenu, N. Margolus, and A. del Campo, Quantum Speed Limits across the Quantum-to-Classical Transition, *Phys. Rev. Lett.* **120**, 070401 (2018).
- [14] A. del Campo, I. L. Egusquiza, M. B. Plenio, and S. F. Huelga, Quantum Speed Limits in Open System Dynamics, *Phys. Rev. Lett.* **110**, 050403 (2013).
- [15] S.-x. Wu and C.-s. Yu, Quantum speed limit for a mixed initial state, *Phys. Rev. A* **98**, 042132 (2018).
- [16] F. Campaioli, F. A. Pollock, F. C. Binder, and K. Modi, Tightening Quantum Speed Limits for Almost All States, *Phys. Rev. Lett.* **120**, 060409 (2018).
- [17] F. Campaioli, F. A. Pollock, and K. Modi, Tight, robust, and feasible quantum speed limits for open dynamics, *Quantum* **3**, 168 (2019).
- [18] S. Sun and Y. Zheng, Distinct Bound of the Quantum Speed Limit via the Gauge Invariant Distance, *Phys. Rev. Lett.* **123**, 180403 (2019).
- [19] S. Sun, Y. Peng, X. Hu, and Y. Zheng, Quantum Speed Limit Quantified by the Changing Rate of Phase, *Phys. Rev. Lett.* **127**, 100404 (2021).
- [20] D. P. Pires, M. Cianciaruso, L. C. Céleri, G. Adesso, and D. O. Soares-Pinto, Generalized Geometric Quantum Speed Limits, *Phys. Rev. X* **6**, 021031 (2016).
- [21] Y. Shao, B. Liu, M. Zhang, H. Yuan, and J. Liu, Operational definition of a quantum speed limit, *Phys. Rev. Research* **2**, 023299 (2020).
- [22] J. Liu, Z. Miao, L. Fu, and X. Wang, Bhatia-Davis formula in the quantum speed limit, *Phys. Rev. A* **104**, 052432 (2021).
- [23] C. Liu, Z.-Y. Xu, and S. Zhu, Quantum-speed-limit time for multiqubit open systems, *Phys. Rev. A* **91**, 022102 (2015).
- [24] A. Chenu, M. Beau, J. Cao, and A. del Campo, Quantum Simulation of Generic Many-Body Open System Dynamics Using Classical Noise, *Phys. Rev. Lett.* **118**, 140403 (2017).
- [25] M. Beau and A. del Campo, Nonlinear Quantum Metrology of Many-Body Open Systems, *Phys. Rev. Lett.* **119**, 010403 (2017).
- [26] M. Bukov, D. Sels, and A. Polkovnikov, Geometric Speed Limit of Accessible Many-Body State Preparation, *Phys. Rev. X* **9**, 011034 (2019).
- [27] G. C. Hegerfeldt, Driving at the Quantum Speed Limit: Optimal Control of a Two-Level System, *Phys. Rev. Lett.* **111**, 260501 (2013).
- [28] S. Deffner and S. Campbell, Quantum speed limits: from Heisenberg's uncertainty principle to optimal quantum control, *J. Phys. A: Math. Theor.* **50**, 453001 (2017).
- [29] M. Beau, J. Kiukas, I. L. Egusquiza, and A. del Campo, Nonexponential Quantum Decay under Environmental Decoherence, *Phys. Rev. Lett.* **119**, 130401 (2017).
- [30] S. Campbell and S. Deffner, Trade-Off Between Speed and Cost in Shortcuts to Adiabaticity, *Phys. Rev. Lett.* **118**, 100601 (2017).
- [31] X. Cai and Y. Zheng, Quantum dynamical speedup in a nonequilibrium environment, *Phys. Rev. A* **95**, 052104 (2017).
- [32] M. Okuyama and M. Ohzeki, Quantum Speed Limit is Not Quantum, *Phys. Rev. Lett.* **120**, 070402 (2018).
- [33] D. Girolami, How Difficult is it to Prepare a Quantum State? *Phys. Rev. Lett.* **122**, 010505 (2019).
- [34] X. Hu, S. Sun, and Y. Zheng, Quantum speed limit via the trajectory ensemble, *Phys. Rev. A* **101**, 042107 (2020).
- [35] S. Becker, N. Datta, L. Lami, and C. Rouzé, Energy-Constrained Discrimination of Unitaries, Quantum Speed Limits, and a Gaussian Solovay-Kitaev Theorem, *Phys. Rev. Lett.* **126**, 190504 (2021).
- [36] G. Ness, M. R. Lam, W. Alt, D. Meschede, Y. Sagi, and

- A. Alberti, Observing crossover between quantum speed limits, *Sci. Adv.* **7**, eabj9119 (2021).
- [37] A. del Campo, Probing Quantum Speed Limits with Ultracold Gases, *Phys. Rev. Lett.* **126**, 180603 (2021).
- [38] G. Ness, A. Alberti, and Y. Sagi, Quantum Speed Limit for States with a Bounded Energy Spectrum, *Phys. Rev. Lett.* **129**, 140403 (2022).
- [39] L. P. García-Pintos, S. B. Nicholson, J. R. Green, A. del Campo, and A. V. Gorshkov, Unifying Quantum and Classical Speed Limits on Observables, *Phys. Rev. X* **12**, 011038 (2022).
- [40] J. Liu, H. Yuan, X.-M. Lu, and X. Wang, Quantum Fisher information matrix and multiparameter estimation, *J. Phys. A: Math. Theor.* **53**, 023001 (2020).
- [41] W. Wu and J.-H. An, Quantum speed limit of a noisy continuous-variable system, *Phys. Rev. A* **106**, 062438 (2022).
- [42] D. Mondal, C. Datta, and S. Sazim, Quantum coherence sets the quantum speed limit for mixed states, *Phys. Lett. A* **380**, 689-695 (2016).
- [43] B. P. Lanyon, P. Jurcevic, M. Zwerger, C. Hempel, E. A. Martinez, W. Dür, H. J. Briegel, R. Blatt, and C. F. Roos, Measurement-Based Quantum Computation with Trapped Ions, *Phys. Rev. Lett.* **111**, 210501 (2013).
- [44] D. Kim, Z. Shi, C. B. Simmons, D. R. Ward, J. R. Prance, T. S. Koh, J. K. Gamble, D. E. Savage, M. G. Lagally, M. Friesen, S. N. Coppersmith, and M. A. Eriksson, Quantum control and process tomography of a semiconductor quantum dot hybrid qubit, *Nature* **511**, 70-74 (2014).
- [45] A. Carlini, A. Hosoya, T. Koike, and Y. Okudaira, Time-Optimal Quantum Evolution, *Phys. Rev. Lett.* **96**, 060503 (2006).
- [46] A. Carlini, A. Hosoya, T. Koike, and Y. Okudaira, Time-optimal unitary operations, *Phys. Rev. A* **75**, 042308 (2007).
- [47] A. Joshi and S. V. Lawande, Generalized Jaynes-Cummings models with a time-dependent atom-field coupling, *Phys. Rev. A* **48**, 2276 (1993).
- [48] S. V. Lawande and A. Joshi, Stochastic fluctuations in the Jaynes-Cummings model, *Phys. Rev. A* **50**, 1692 (1994).
- [49] L. Du, Y.-T. Chen, Y. Zhang, and Y. Li, Giant atoms with time-dependent couplings, *Phys. Rev. Research* **4**, 023198 (2022).
- [50] M. O. Scully and M. S. Zubairy, *Quantum Optics* (Cambridge University Press, Cambridge, England, 1997).
- [51] C. N. Madsen, L. Valdetaro, and K. Mølmer, Quantum estimation of a time-dependent perturbation, *Phys. Rev. A* **104**, 052621 (2021).
- [52] G. Carleo and M. Troyer, Solving the quantum many-body problem with artificial neural networks, *Science* **355**, 602-606 (2017).
- [53] M. J. Hartmann and G. Carleo, Neural-Network Approach to Dissipative Quantum Many-Body Dynamics, *Phys. Rev. Lett.* **122**, 250502 (2019).
- [54] M. Schmitt and M. Heyl, Quantum Many-Body Dynamics in Two Dimensions with Artificial Neural Networks *Phys. Rev. Lett.* **125**, 100503 (2020).
- [55] E. Flurin, L. S. Martin, S. Hacoen-Gourgy, and I. Siddiqi, Using a Recurrent Neural Network to Reconstruct Quantum Dynamics of a Superconducting Qubit from Physical Observations, *Phys. Rev. X* **10**, 011006 (2020).
- [56] V. V. Sivak, A. Eickbusch, H. Liu, B. Royer, I. Tsioutsios, and M. H. Devoret, Model-Free Quantum Control with Reinforcement Learning, *Phys. Rev. X* **12**, 011059 (2022).
- [57] The actual computing time is less than the evaluation since parallel computing is applied.
- [58] S. J. van Enk and C. W. J. Beenakker, Measuring  $\text{Tr}\rho^n$  on Single Copies of  $\rho$  Using Random Measurements, *Phys. Rev. Lett.* **108**, 110503 (2012).
- [59] A. Elben, B. Vermersch, R. van Bijnen, C. Kokail, T. Brydges, C. Maier, M. K. Joshi, R. Blatt, C. F. Roos, and P. Zoller, Cross-Platform Verification of Intermediate Scale Quantum Devices, *Phys. Rev. Lett.* **124**, 010504 (2020).
- [60] J. R. Johansson, P. D. Nation, and F. Nori, QuTiP: An open-source Python framework for the dynamics of open quantum systems, *Comp. Phys. Comm.* **183**, 1760 (2012).
- [61] F. Pedregosa, G. Varoquaux, A. Gramfort, V. Michel, B. Thirion, O. Grisel, M. Blondel, P. Prettenhofer, R. Weiss, V. Dubourg, J. Vanderplas, A. Passos, D. Cournapeau, M. Brucher, M. Perrot, and É. Duchesnay, Scikit-learn: Machine Learning in Python, *J. Mach. Learn. Res.* **12**, 2825 (2011).
- [62] J. R. Johansson, P. D. Nation, and F. Nori, QuTiP 2: A Python framework for the dynamics of open quantum systems, *Comp. Phys. Comm.* **184**, 1234 (2013).
- [63] M. Fishman, S. R. White, E. M. Stoudenmire, The ITensor Software Library for Tensor Network Calculations, *SciPost Phys. Codebases* **4** (2022).
- [64] E. B. Baum and F. Wilczek, *Supervised learning of probability distributions by neural networks* (American Institute of Physics, New York, 1988).
- [65] D. P. Kingma and J. Ba, Adam: A Method for Stochastic Optimization, *arXiv:1412.6980*.
- [66] E. L. Lehmann and G. Casella, *Theory of Point Estimation* (Springer, New York, 1998).
- [67] M. Zhang, H.-M. Yu, H. Yuan, X. Wang, R. Demkowicz-Dobrzański, and J. Liu, QuanEstimation: An open-source toolkit for quantum parameter estimation, *Phys. Rev. Research* **4**, 043057 (2022).
- [68] M. Innes, Don't Unroll Adjoint: Differentiating SSA-form programs, *arXiv:1810.07951*.
- [69] M. A. Nielsen and I. L. Chuang, *Quantum Computation and Quantum Information* (Cambridge University Press, Cambridge, 2000).

### Acknowledgments

The authors thank Yuqian Xu for helpful discussion. This work was supported by the National Natural Science Foundation of China (Grant No. 12175075).

### Author contributions

J.L. conceived the idea and wrote the manuscript. M.Z. and H.M.Y. performed the calculations. All authors contributed to the discussion and reviewed the manuscript.

### Competing interests

The authors declare no competing interests.



## Appendix A: Connections between different tools to define the target

It is well known that there exist various types of tools in the quantum speed limit (QSL) to define the target, and different tools may lead to different mathematical bounds or methods for the description of QSL. However, it is possible that a physical target could be quantified via different tools, and thus these tools should present connections on values. For example, assume the target is defined by the tool  $\Phi_1$  and a specific value (denoted by  $\phi$ ) of it is taken as the target, then this target can also be represented by another tool  $\Phi_2$  as long as  $\Phi_1$  and  $\Phi_2$  have certain connections on values. Denote this connection as a function, i.e.,  $\Phi_2 = f(\Phi_1)$ , then with the tool of  $\Phi_2$  the target value can be expressed by  $f(\Phi_1 = \phi)$ . When the connection is a one-to-one correspondence, namely,  $f$  is an univalent function, the targets  $\phi$  and  $f(\Phi_1 = \phi)$  are equivalent. In the case that  $f$  is a multivalent function, this conversion would lead to several different target values.

Now we discuss the relation between the angle of relative purity and Bloch angle as a demonstration. In the perspective of QSL, the angle ( $\Phi \in (0, \pi/2]$ ) of relative purity could be defined by

$$\Phi = \arccos\left(\frac{\text{Tr}(\rho\rho(t))}{\text{Tr}(\rho^2)}\right), \quad (\text{A1})$$

where  $\rho$  is the initial state and  $\rho(t)$  is the corresponding evolved state at time  $t$ . In the Bloch representation,  $\rho$  can be expressed by

$$\rho = \frac{1}{N} \left( \mathbb{1} + \sqrt{\frac{N(N-1)}{2}} \vec{r} \cdot \vec{\lambda} \right), \quad (\text{A2})$$

where  $N$  is the dimension of  $\rho$ ,  $\vec{\lambda}$  is the vector of  $\text{SU}(N)$  generators and its  $i$ th entry  $\lambda_i$  and  $j$ th entry  $\lambda_j$  satisfies  $\text{Tr}(\lambda_i \lambda_j) = 2\delta_{ij}$  with  $\delta_{ij}$  the Kronecker delta function.  $\vec{r}$  is the Bloch vector satisfying  $|\vec{r}| \leq 1$ .  $\mathbb{1}$  is the identity matrix. Substituting Eq. (A2) into Eq. (A1), one can obtain

$$\frac{\text{Tr}(\rho\rho(t))}{\text{Tr}(\rho^2)} = \frac{1 + (N-1)\vec{r} \cdot \vec{r}(t)}{1 + (N-1)|\vec{r}|^2}. \quad (\text{A3})$$

In the perspective of QSL, the Bloch angle  $\theta \in (0, \pi]$  is defined as the angle between the vectors  $\vec{r}$  and  $\vec{r}(t)$ . Hence, Eq. (A3) can be rewritten into

$$\cos \Phi = \frac{1 + (N-1)|\vec{r}|^2 \cos \theta}{1 + (N-1)|\vec{r}|^2}, \quad (\text{A4})$$

where  $\cos \theta \geq \max\left\{-1, -\frac{1}{(N-1)|\vec{r}|^2}\right\}$ . This condition is to guarantee that the right-hand term in the equation is non-negative. As demonstrated in Fig. 4, for the same initial state  $\theta$  and  $\Phi$  has a one-to-one correspondence relation and thus they are equivalent on values.

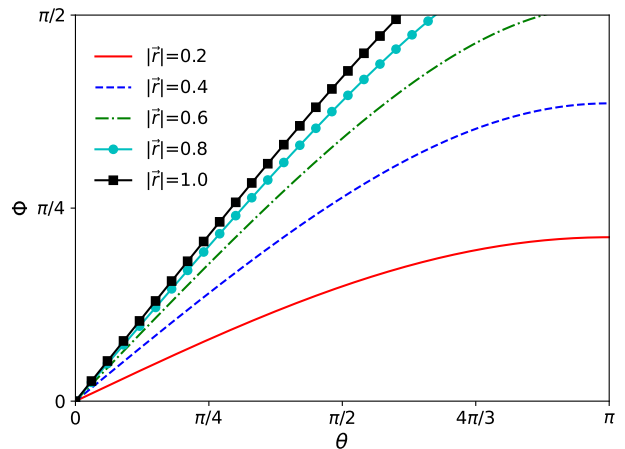


Figure 4. Demonstration of the one-to-one correspondence between the angle of relative purity and Bloch angle for the states with  $|\vec{r}| = 0.2$  (solid-red line),  $|\vec{r}| = 0.4$  (dashed-blue line),  $|\vec{r}| = 0.6$  (dash-dotted-green line),  $|\vec{r}| = 0.8$  (solid-cyan-circle line), and  $|\vec{r}| = 1.0$  (solid-black-square line), respectively.  $N = 4$  in the plot.

In the perspective of the operational definition of quantum speed limit (OQSL), this one-to-one correspondence means that the set of target states for the same initial state are exactly the same for these two tools, and hence the reachable state sets of them are also the same, indicating that they are actually the same problem. For the tools that no one-to-one correspondence exists, such as the Bures angle and Bloch angle, the reachable state sets are not exactly the same for these tools and the result of OQSL may not be the same.

## Appendix B: Connection between the OQSL and the quantum brachistochrones problem

The OQSL has a deep connection with the quantum brachistochrones problem. In the problem of quantum brachistochrones, people usually concern about the minimum time for a given initial state to a target state  $\rho_{\text{tar}}$  or the realization of a certain gate. Due to the fact that in OQSL the initial state has been optimized, instead of a given initial state, with the OQSL we can study the minimum time for a set of initial states (denoted by  $\mathcal{Q}$ ) to reach the target state. Notice that if  $\rho_{\text{tar}} \in \mathcal{Q}$ , the optimal state in  $\mathcal{Q}$  to reach  $\rho_{\text{tar}}$  must be  $\rho_{\text{tar}}$  itself for any Hamiltonian and the corresponding time is nothing but zero, indicating that this is a trivial case. Therefore, here we only consider the nontrivial case that  $\rho_{\text{tar}} \notin \mathcal{Q}$  is satisfied. Next we take a qubit case as a demonstration.

Consider a noncontrolled Hamiltonian  $H = \omega\sigma_z/2$  with  $\sigma_z$  the Pauli Z matrix and  $\omega$  the energy difference. The other two Pauli matrices are denoted by  $\sigma_x$  and  $\sigma_y$ . The target state  $\rho_{\text{tar}} = (|0\rangle - |1\rangle)/\sqrt{2}$  with  $|0\rangle$  ( $|1\rangle$ ) the eigenstate of  $\sigma_z$  corresponding to the eigenvalue 1 ( $-1$ ). The set  $\mathcal{Q} = \{\rho | \text{Tr}(\rho\sigma_x) \geq 0\}$ . In this case, the reachable

state set can be written as

$$\mathcal{S} = \{\rho | \rho \in \mathcal{Q} \ \& \ e^{-iHt} \rho e^{iHt} = \rho_{\text{tar}}, \exists t\}. \quad (\text{B1})$$

In the Bloch representation with  $|0\rangle$  the north pole  $[\vec{r} = (r_x, r_y, r_z)^T]$ ,  $\mathcal{Q}$  can be rewritten into  $\mathcal{Q} = \{\vec{r} | r_x \geq 0\}$  and the equation  $e^{-iHt} \rho e^{iHt} = \rho_{\text{tar}}$  can be rewritten into

$$\begin{cases} \frac{1}{2}(1 + r_z) = \frac{1}{2}, \\ \frac{1}{2}e^{-i\omega t}(r_x - ir_y) = -\frac{1}{2}. \end{cases} \quad (\text{B2})$$

To make sure that these equations have legitimate solutions of time,  $\vec{r}$  has to satisfy the conditions  $r_z = 0$  and  $r_x^2 + r_y^2 = 1$ . Hence,  $\mathcal{S}$  can be expressed by

$$\mathcal{S} = \{\vec{r} | r_z = 0, r_x \geq 0, r_x^2 + r_y^2 = 1\}. \quad (\text{B3})$$

Utilizing the spherical coordinates of  $\vec{r}$ , i.e.,

$$\vec{r} = \eta(\sin \alpha \cos \varphi, \sin \alpha \sin \varphi, \cos \alpha)^T \quad (\text{B4})$$

with  $\alpha \in [0, \pi]$  and  $\varphi \in [0, 2\pi)$ ,  $\mathcal{S}$  can be rewritten into

$$\mathcal{S} = \{\vec{r} | \eta = 1, \alpha = \pi/2, \varphi \in [0, \pi/2] \cup [3\pi/2, 2\pi)\}. \quad (\text{B5})$$

The solution of time for Eq. (B2) is

$$t = \frac{(2k+1)\pi - \varphi}{\omega}, k = 0, 1, 2, \dots \quad (\text{B6})$$

The minimum time  $\tau = \pi/(2\omega)$ , which can be attained by the state  $(0, 1, 0)^T$ .

This result is quite reasonable from the perspective of geometry. As a matter of fact,  $\mathcal{S}$  is nothing but half of the  $xy$  plane with  $r_x \geq 0$ . Due to the fact that the dynamics is the rotation about  $z$  axis, the state that can reach the target state  $(-1, 0, 0)^T$  in the minimum time to is just the  $y$  axis, i.e.,  $(0, 1, 0)^T$ .

### Appendix C: The OQSL for time-dependent Hamiltonian with time-independent eigenstates

#### 1. Proof of the Theorem

Consider the time-dependent Hamiltonian of the form

$$H(t) = \sum_i E_i(t) |E_i\rangle \langle E_i|, \quad (\text{C1})$$

where the energies are assumed to be ordered ascendingly, i.e.,  $E_0(t) \leq E_1(t) \leq \dots \leq E_{N-1}(t)$  (not all the equalities are saturated simultaneously) and  $|E_i\rangle$  is independent of the time for any subscript  $i$ . With this Hamiltonian, the OQSL  $\tau$  satisfies

$$\int_0^\tau E_{N-1}(t) - E_0(t) dt = \Theta, \quad (\text{C2})$$

where  $E_{N-1}(t)$  and  $E_0(t)$  are the highest and lowest energies of the Hamiltonian at time  $t$ . The proof is as follows.

In the case of unitary dynamics, any  $SU(N)$  generator satisfies  $U(t)\lambda_i U^\dagger(t) = \sum_j C_{ij}(t)\lambda_j$  with  $U(t)$  a unitary operator, then the dynamics of  $\vec{r}$  can be written as  $\vec{r}(t) = C^T(t)\vec{r}$ . Due to the polar decomposition,  $C^T$  can be decomposed into  $C^T = OS$  with  $O$  a real orthogonal matrix and  $S$  a real positive semi-definite symmetric matrix. Hence,  $C^T$  represents a deformation of the Bloch sphere along principal axes determined by  $S$  and then a proper rotation due to  $O$  [69]. Recall that  $\text{Tr}(\lambda_i \lambda_j) = 2\delta_{ij}$  with  $\delta_{ij}$  the Kronecker delta function, then  $C_{ij}(t)$  can be further solved as  $C_{ij}(t) = \text{Tr}(U(t)\lambda_i U^\dagger(t)\lambda_j)/2$ .

With the Hamiltonian (C1), the unitary operator can be expressed by

$$\begin{aligned} U(t) &= e^{-i \sum_m \int_0^t E_m(t_1) dt_1} |E_m\rangle \langle E_m| \\ &= \sum_m e^{-i \int_0^t E_m(t_1) dt_1} |E_m\rangle \langle E_m|, \end{aligned} \quad (\text{C3})$$

which indicates

$$C_{ij}(t) = \frac{1}{2} \sum_{mn} e^{i \int_0^t E_m(t_1) - E_n(t_1) dt_1} [\lambda_i]_{mn}^* [\lambda_j]_{mn} \quad (\text{C4})$$

with  $[\lambda_j]_{mn}$  the  $m$ th entry of  $\lambda_j$ . In the energy basis  $\{|E_0\rangle, |E_1\rangle, \dots, |E_{N-1}\rangle\}$ ,  $C(t)$  has the same structure with the time-dependent Hamiltonian [21], i.e.,

$$C(t) = \bigoplus_{n=1}^{N-1} V(n, t), \quad (\text{C5})$$

where  $V(n, t) = \left[ \bigoplus_{i=0}^{n-1} M(\Delta_{ni}) \right] \oplus 1$  with

$$M(x) = \begin{pmatrix} \cos x & -\sin x \\ \sin x & \cos x \end{pmatrix} \quad (\text{C6})$$

and  $\Delta_{ni} = \int_0^t E_n(t_1) - E_i(t_1) dt_1$ . Then the angle between the initial and evolved Bloch vectors is

$$\cos \theta = \frac{\vec{r}(t) \cdot \vec{r}}{|\vec{r}|^2} = \frac{\vec{r}^T C(t) \vec{r}}{|\vec{r}|^2}. \quad (\text{C7})$$

Utilizing Eq. (C5), it can be further calculated as

$$\cos \theta = 1 - \frac{1}{|\vec{r}|^2} \sum_{n=1}^{N-1} \sum_{i=0}^{n-1} [1 - \cos(\Delta_{ni})] (r_{n^2+2i-1}^2 + r_{n^2+2i}^2)$$

with  $r_i$  the  $i$ th element of  $\vec{r}$ . Hence, the set  $\mathcal{S}$  can be directly expressed by

$$\begin{aligned} \mathcal{S} &= \left\{ \vec{r} \mid 1 - \cos \Theta = \frac{1}{|\vec{r}|^2} \sum_{n=1}^{N-1} \sum_{i=0}^{n-1} [1 - \cos(\Delta_{ni})] \right. \\ &\quad \left. \times (r_{n^2+2i-1}^2 + r_{n^2+2i}^2), \exists t \right\}. \end{aligned} \quad (\text{C8})$$

To further obtain the OQSL, the two-step proof strategy used in Appendix B in Ref. [21] needs to be applied. Define

$$f(t) := \frac{1}{|\vec{r}|^2} \sum_{n=1}^{N-1} \sum_{i=0}^{n-1} [1 - \cos(\Delta_{ni})] (r_{n^2+2i-1}^2 + r_{n^2+2i}^2).$$

Substituting the equation

$$\int_0^\tau E_{N-1}(t) - E_0(t) dt = \Theta \quad (\text{C9})$$

into the expression of  $f(t)$ , it can be seen that

$$\left. \frac{\partial f(t)}{\partial t} \right|_{t=\tau} \geq 0, \quad (\text{C10})$$

which indicates  $\tau$  is in the first monotonic increasing regime of  $f(t)$ . In the meantime, it can also be found that  $f(\tau) \leq 1 - \cos \Theta$ , which is due to the fact

$$\begin{aligned} f(\tau) &\leq (1 - \cos \Theta) \sum_{n=1}^{N-1} \sum_{i=0}^{n-1} \frac{r_{n^2+2i-1}^2 + r_{n^2+2i}^2}{|\vec{r}|^2} \\ &\leq 1 - \cos \Theta. \end{aligned} \quad (\text{C11})$$

Here the inequality  $1 - \cos(\Delta_{ni}(\tau)) \leq 1 - \cos \Theta$  has been applied. If the solution of  $f(t) = 1 - \cos \Theta$  is not in the first increasing regime of  $f(t)$ , then  $t$  is obviously larger than  $\tau$ ; if this solution is in the first increasing regime, then due to  $f(\tau) \leq 1 - \cos \Theta = f(t)$  one can also see that  $t \geq \tau$ . Hence,  $\tau$  is a lower bound of the time to reach the target angle.

Now we discuss the optimal probe states to reach the OQSL. To let the equation  $1 - \cos \Theta = f(\tau)$  holds, the term  $r_{n^2+2i-1}^2 + r_{n^2+2i}^2$  for the subscripts  $n, i$  satisfying  $\Delta_{ni} \neq \int_0^\tau E_{N-1}(t) - E_0(t) dt$  has to vanish. Further assume the degeneracy of the ground states and highest excited states are  $p$  and  $q$ , namely,  $E_0(t) = E_1(t) = \dots = E_{p-1}(t)$  and  $E_{N-q}(t) = E_{N-q+1}(t) = \dots = E_{N-1}(t)$ , then it is easy to see that  $r_{n^2+2i-1}^2 + r_{n^2+2i}^2$  can only be nonzero when  $n \in [N-q, N-1]$  and  $i \in [0, p-1]$ , which indicates that the optimal state is of the form

$$\sum_{i=0}^{N-1} \frac{1}{N} |E_i\rangle \langle E_i| + \sum_{\substack{k \in [0, p-1], \\ l \in [N-q, N-1]}} \xi_{kl} |E_k\rangle \langle E_l| + \xi_{kl}^* |E_l\rangle \langle E_k|, \quad (\text{C12})$$

where  $\xi_{kl} = \sqrt{\frac{N-1}{2N}} (r_{l^2+2k-1} - ir_{l^2+2k})$ . In the energy basis  $\{|E_0\rangle, |E_1\rangle, \dots, |E_{N-1}\rangle\}$ , the state above can be written as

$$\frac{1}{N} \mathbb{1} + \begin{pmatrix} 0 & 0 & \xi \\ 0 & \dots & 0 \\ \xi^\dagger & 0 & 0 \end{pmatrix}, \quad (\text{C13})$$

where  $\mathbb{1}$  is a  $N$ -dimensional identity matrix, and  $\xi$  is a  $p$  by  $q$  matrix with  $kl$ th entry  $\xi_{kl}$ . To make sure the

density matrix is positive-semidefinite, according to the Schur complement theorem  $\xi$  needs to satisfy

$$\xi^\dagger \xi \leq \frac{1}{N^2} \mathbb{1}_q, \quad (\text{C14})$$

where  $\mathbb{1}_q$  is a  $q$ -dimensional identity matrix. The theorem is then proved.  $\blacksquare$

## 2. Example: two-level systems

Here we take a two-level system as a demonstration of the Theorem. Consider the Hamiltonian

$$H(t) = f(t) \sigma_z, \quad (\text{C15})$$

where  $f(t)$  is a function of time  $t$ , and  $\sigma_z$  is the Pauli  $Z$  matrix. In the Bloch representation, the evolved Bloch vector can be solved as

$$\begin{aligned} r_x(t) &= r_x \cos \left[ 2 \int_0^t f(t_1) dt_1 \right] - r_y \sin \left[ 2 \int_0^t f(t_1) dt_1 \right], \\ r_y(t) &= r_x \sin \left[ 2 \int_0^t f(t_1) dt_1 \right] + r_y \cos \left[ 2 \int_0^t f(t_1) dt_1 \right], \\ r_z(t) &= r_z, \end{aligned}$$

where  $(r_x, r_y, r_z)^\text{T} = \vec{r}$  is the Bloch vector of the initial state. Based on this dynamics, the angle between the initial and evolved states is

$$\cos \theta = \frac{\cos \left[ 2 \int_0^t f(t_1) dt_1 \right] (r_x^2 + r_y^2) + r_z^2}{|\vec{r}|^2}, \quad (\text{C16})$$

which indicates that the time to reach the target angle  $\Theta$  satisfies the following equation

$$\sin^2 \left[ \int_0^t f(t_1) dt_1 \right] = \frac{|\vec{r}|^2}{|\vec{r}|^2 - r_z^2} \sin^2 \left( \frac{\Theta}{2} \right). \quad (\text{C17})$$

Rewrite  $\vec{r}$  into

$$\vec{r} = \eta (\sin \alpha \cos \varphi, \sin \alpha \sin \varphi, \cos \alpha)^\text{T} \quad (\text{C18})$$

with  $\eta \in [0, 1]$ ,  $\alpha \in [0, \pi]$  and  $\varphi \in [0, 2\pi]$ , and Eq. (C17) reduces to

$$\sin^2 \alpha = \frac{\sin^2 \left( \frac{\Theta}{2} \right)}{\sin^2 \left[ \int_0^t f(t_1) dt_1 \right]}. \quad (\text{C19})$$

Now consider that  $|\int_0^t f(t_1) dt_1|$  is upper bounded by  $c_f$ , then in the case that  $c_f < \Theta/2$ ,  $\sin^2 \left[ \int_0^t f(t_1) dt_1 \right]$  is always less than  $\sin^2(\Theta/2)$ , which gives  $\sin^2 \alpha > 1$ . This means no state can fulfill the target as  $\sin^2 \alpha$  is always equal or less than 1. In the case that  $c_f \in [\Theta/2, \pi/2]$ ,

$$\sin^2 \left[ \int_0^t f(t_1) dt_1 \right] \leq \sin^2 c_f \leq 1. \quad (\text{C20})$$

Hence,

$$\sin^2 \alpha \geq \frac{\sin^2(\frac{\Theta}{2})}{\sin^2 c_f}, \quad (\text{C21})$$

indicating that the states that can fulfill the target satisfies  $\alpha \in [\alpha_f, \pi - \alpha_f]$  with

$$\alpha_f = \arcsin\left(\frac{\sin(\frac{\Theta}{2})}{\sin c_f}\right). \quad (\text{C22})$$

In the case that  $c_f > \pi/2$ ,  $\sin^2[\int_0^t f(t_1)dt_1]$  can reach all the values between 0 and 1, and  $\sin^2 \alpha \geq \sin^2(\Theta/2)$ , therefore, the states satisfies  $\alpha \in [\Theta/2, \pi - \Theta/2]$ . In a word, the set  $\mathcal{S}$  can be expressed by

$$\mathcal{S} = \begin{cases} \emptyset, & c_f < \frac{\Theta}{2}, \\ \{\vec{r} \mid \alpha \in [\alpha_f, \pi - \alpha_f]\}, & c_f \in [\frac{\Theta}{2}, \frac{\pi}{2}], \\ \{\vec{r} \mid \alpha \in [\frac{\Theta}{2}, \pi - \frac{\Theta}{2}]\}, & c_f > \frac{\pi}{2}. \end{cases} \quad (\text{C23})$$

Here  $\emptyset$  is the empty set, and in the second and third circumstances  $\eta \in (0, 1]$  and  $\varphi \in [0, 2\pi]$ .

With respect to the OQSL, due to the fact that the eigenvalues are always  $f(t)$  and  $-f(t)$ , the maximum and minimum ones are always  $|f(t)|$  and  $-|f(t)|$ , respectively. Based on the Theorem, the OQSL  $\tau$  then satisfies

$$\int_0^\tau |f(t)|dt = \frac{\Theta}{2}. \quad (\text{C24})$$

A physical example for the Hamiltonian (C15) is the energy splitting coming from Zeeman effect, i.e.,

$$f(t) = -\frac{g\mu_B}{2}B(t) \quad (\text{C25})$$

with  $g$  the Lande factor and  $\mu_B$  the electron magnetic moment.  $B(t)$  is the time-dependent magnetic field. For a periodic magnetic field  $B(t) = B \cos(\omega t)$  with  $B, \omega > 0$ , it is easy to see

$$\left| \int_0^t f(t_1)dt_1 \right| = \left| \frac{g\mu_B B}{2\omega} \sin(\omega t) \right| \leq \frac{g\mu_B B}{2\omega}. \quad (\text{C26})$$

According to Eq. (C23), the set  $\mathcal{S}$  reads

$$\mathcal{S} = \begin{cases} \emptyset, & \frac{g\mu_B B}{2\omega} < \frac{\Theta}{2}, \\ \{\vec{r} \mid \alpha \in [\alpha_f, \pi - \alpha_f]\}, & \frac{g\mu_B B}{2\omega} \in [\frac{\Theta}{2}, \frac{\pi}{2}], \\ \{\vec{r} \mid \alpha \in [\frac{\Theta}{2}, \pi - \frac{\Theta}{2}]\}, & \frac{g\mu_B B}{2\omega} > \frac{\pi}{2}. \end{cases} \quad (\text{C27})$$

Here  $\eta \in (0, 1]$ ,  $\varphi \in [0, 2\pi]$  and

$$\alpha_f = \arcsin\left(\frac{\sin(\frac{\Theta}{2})}{\sin(\frac{g\mu_B B}{2\omega})}\right). \quad (\text{C28})$$

Utilizing the Theorem, Eq. (C24) can be written as

$$\int_0^\tau |\cos(\omega t)|dt = \frac{\Theta}{g\mu_B B}. \quad (\text{C29})$$

In the case that  $\frac{g\mu_B B}{2\omega} < \frac{\Theta}{2}$ ,  $\tau = \infty$  as no states can reach the target. Hence we only consider the non-trivial case that  $\frac{g\mu_B B}{2\omega} \geq \frac{\Theta}{2}$ , which means  $\frac{\Theta}{g\mu_B B} \leq \frac{1}{\omega}$ , and therefore  $\int_0^\tau |\cos(\omega t)|dt \leq 1/\omega$ , namely,  $\int_0^\tau |\cos(\omega t)|d(\omega t) \leq 1$ . The integration of  $|\cos(\omega t)|$  is only less or equal to 1 when  $\omega t \leq \pi/2$ , in which regime  $\cos(\omega t)$  is always non-negative, hence, the integration is equivalent to be performed on  $\cos(\omega t)$ . Finally, the equation above can be rewritten into

$$\int_0^\tau \cos(\omega t)dt = \frac{\Theta}{g\mu_B B}, \quad (\text{C30})$$

which immediately gives the analytical expression of  $\tau$  as below

$$\tau = \frac{1}{\omega} \arcsin\left(\frac{\omega\Theta}{g\mu_B B}\right). \quad (\text{C31})$$

An interesting fact in this case is that the first degenerate point shows at  $t = \pi/(2\omega)$ , and the OQSL is always less or equal to this time, indicating that the target  $\Theta$ , regardless of its value, can always be reached before this first degeneracy point.

Next we consider a controlled case that

$$f(t) = -\frac{g\mu_B}{2}B \cos(\omega t) + u(t), \quad (\text{C32})$$

where  $|u(t)| \leq u_b$  is a bounded control. Since

$$\begin{aligned} & \left| \int_0^t -\frac{g\mu_B}{2}B \cos(\omega t_1) + u(t_1)dt_1 \right| \\ &= \left| \frac{g\mu_B B}{2\omega} \sin(\omega t) - \int_0^t u(t_1)dt_1 \right| \\ &\leq \frac{g\mu_B B}{2\omega} + \left| \int_0^t u(t_1)dt_1 \right| \\ &\leq \frac{g\mu_B B}{2\omega} + u_b t, \end{aligned} \quad (\text{C33})$$

which can be larger than  $\pi/2$  for a long enough time, in this case

$$\mathcal{S} = \left\{ \vec{r} \mid \alpha \in \left[ \frac{\Theta}{2}, \pi - \frac{\Theta}{2} \right] \right\}. \quad (\text{C34})$$

The OQSL here satisfies

$$\int_0^\tau \left| \frac{g\mu_B B}{2} \cos(\omega t) - u(t) \right| dt = \frac{\Theta}{2}. \quad (\text{C35})$$

Then the minimum value of  $\tau$  (denoted by  $\tau_{\min}$ ) can be solved via the problem

$$\begin{aligned} \tau_{\min} &= \min_{u(t)} \tau, \\ &\text{subject to } \begin{cases} \int_0^\tau | \frac{g\mu_B B}{2} \cos(\omega t) - u(t) | dt = \frac{\Theta}{2}, \\ |u(t)| \leq u_b. \end{cases} \end{aligned}$$

This problem can be solved by maximizing the function  $|\frac{1}{2}g\mu_B B \cos(\omega t) - u(t)|$  under the constraint that its integration is fixed. Since  $\cos(\omega t)$  is a monotonic function within the regime  $[0, \pi/(2\omega)]$ , one could have

$$\begin{aligned} & \int_0^{\frac{\pi}{2\omega}} \left| \frac{g\mu_B B}{2} \cos(\omega t) - u(t) \right| dt \\ & \leq \int_0^{\frac{\pi}{2\omega}} \left[ \frac{g\mu_B B}{2} \cos(\omega t) + u_b \right] dt \\ & = \frac{g\mu_B B}{2\omega} + \frac{\pi}{2\omega} u_b. \end{aligned} \quad (\text{C36})$$

Notice the condition to make sure  $\mathcal{S} \neq \emptyset$  is  $\frac{g\mu_B B}{2\omega} \geq \frac{\Theta}{2}$ . In this case, the upper bound of  $\int_0^{\frac{\pi}{2\omega}} |\frac{g\mu_B B}{2} \cos(\omega t) - u(t)| dt$  is larger than  $\Theta/2$ , indicating that the integration will reach  $\Theta/2$  before the time  $\pi/(2\omega)$  with proper controls. Hence,  $\tau_{\min}$  must be less than  $\pi/(2\omega)$ . Under this condition, the maximum value of  $|\frac{1}{2}g\mu_B B \cos(\omega t) - u(t)|$  is attained when  $u(t) \equiv -u_b$  due to the fact that  $\cos(\omega t)$  is a monotonic function here. Therefore,  $\tau_{\min}$  satisfies the equation

$$\frac{g\mu_B B}{2\omega} \sin(\omega\tau_{\min}) + u_b \tau_{\min} = \frac{\Theta}{2}. \quad (\text{C37})$$

If  $\omega$  is small,  $\tau_{\min}$  approximates to

$$\tau_{\min} \approx \frac{\Theta}{g\mu_B B + 2u_b}. \quad (\text{C38})$$

### 3. Example: one-dimensional Ising model with a longitudinal field

#### a. Periodic boundary condition

In the following we consider the one-dimensional Ising model with a longitudinal field. The Hamiltonian of this system reads

$$H/J = - \sum_{j=1}^n \sigma_j^z \sigma_{j+1}^z - \sum_{j=1}^n g(t) \sigma_j^z, \quad (\text{C39})$$

where  $J > 0$  is the interaction strength of the nearest-neighbor coupling, and  $g(t)$  is a global time-dependent longitudinal field.  $\sigma_j^z$  is the Pauli Z matrix for  $j$ th spin. The Hamiltonian satisfies the periodic boundary condition  $\sigma_{n+1}^z = \sigma_1^z$ . Here we only consider the case that  $n \geq 3$ .

Now we calculate the maximum and minimum eigenvalues of  $H/J$ . Since the Hamiltonian only contains the Pauli Z matrix, it is naturally a diagonal matrix in the space consisting of the eigenspaces of  $\sigma_j^z$  for all  $j$ . Denote  $|\uparrow_j\rangle$  and  $|\downarrow_j\rangle$  as the eigenstates of  $\sigma_j^z$  with respect to the eigenvalues 1 and  $-1$ , then the eigenvalues of  $-\sigma_j^z \sigma_{j+1}^z - g(t) \sigma_j^z$  are  $1 + g(t)$ ,  $1 - g(t)$ ,  $-1 - g(t)$ , and  $-1 + g(t)$ , and the corresponding eigenstates are

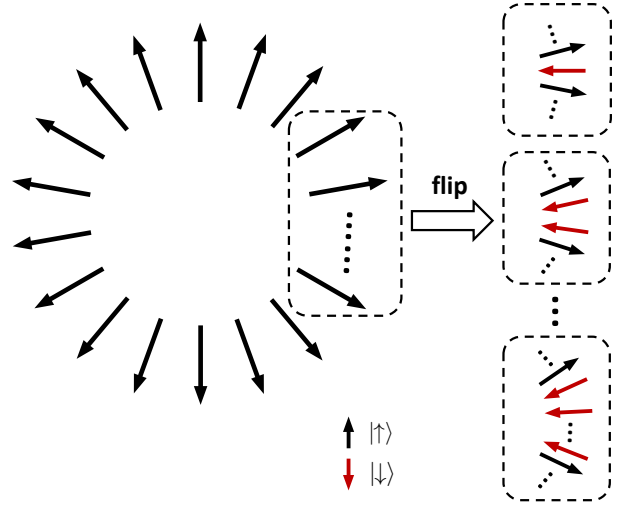


Figure 5. Schematic of obtaining any eigenstate of  $H/J$  by flipping any number of  $|\uparrow\rangle$  (black up arrow) into  $|\downarrow\rangle$  (red down arrow) in the state  $|\uparrow\rangle^{\otimes n}$ .

$|\downarrow_j \uparrow_{j+1}\rangle$ ,  $|\uparrow_j \downarrow_{j+1}\rangle$ ,  $|\uparrow_j \uparrow_{j+1}\rangle$ , and  $|\downarrow_j \downarrow_{j+1}\rangle$ . The eigenvalues of  $H/J$  can be obtained by the summation of a certain number of these four terms. For instance, the eigenvalue with respect to the eigenstate  $|\uparrow\rangle^{\otimes n}$  is  $\sum_{j=1}^n [-1 - g(t)] = n[-1 - g(t)]$ .

Regarding the minimum eigenvalue of  $H/J$ , it is easy to see that the minimum eigenvalue of  $-\sigma_j^z \sigma_{j+1}^z - g(t) \sigma_j^z$  is  $-1 - g(t)$  when  $g(t) \geq 0$  and  $-1 + g(t)$  when  $g(t) \leq 0$ , namely,  $-1 - |g(t)|$ . Therefore, the minimum eigenvalue of  $H/J$  is

$$E_{\min, p} = -n [1 + |g(t)|], \quad (\text{C40})$$

which can be attained by the eigenstate  $|\uparrow\rangle^{\otimes n}$  when  $g(t) \geq 0$  and  $|\downarrow\rangle^{\otimes n}$  when  $g(t) \leq 0$ .

Next, we calculate the maximum eigenvalue. For an eigenstate  $\otimes_{j=1}^n |a_j\rangle$  ( $a_j = \uparrow, \downarrow$ ), denote the number of  $|\uparrow_j \uparrow_{j+1}\rangle$ ,  $|\downarrow_j \downarrow_{j+1}\rangle$ ,  $|\downarrow_j \uparrow_{j+1}\rangle$ , and  $|\uparrow_j \downarrow_{j+1}\rangle$  ( $j \in [1, N]$ ) are  $x_1$ ,  $x_2$ ,  $x_3$ , and  $x_4$ , respectively. For example, for the state  $|\uparrow \downarrow \uparrow\rangle$ ,  $x_1 = 1$ ,  $x_2 = 0$ , and  $x_3 = x_4 = 1$ . Notice that any eigenstate of  $H/J$  can be obtained by flipping any number of  $|\uparrow\rangle$  in the state  $|\uparrow\rangle^{\otimes n}$  into  $|\downarrow\rangle$ . As long as the number of flipped spins is less than  $n$ , no matter how many spins are flipped, there always exists a pair of  $|\uparrow \downarrow\rangle$  and  $|\downarrow \uparrow\rangle$  at the boundary of the flipped spins, as shown in Fig. 5. For example, assume a flip occurs at the  $j$ th spin and  $k$  spins are flipped. Then the state of the  $(j-1)$ th and  $j$ th spins must be  $|\uparrow_{j-1} \downarrow_j\rangle$ , and that of the  $(j+k-1)$ th and  $(j+k)$ th spins must be  $|\downarrow_{j+k-1} \uparrow_{j+k}\rangle$ . If all the spins are flipped, no  $|\uparrow \downarrow\rangle$  and  $|\downarrow \uparrow\rangle$  exist in the state. The simultaneous existence of  $|\uparrow \downarrow\rangle$  and  $|\downarrow \uparrow\rangle$  in the flip indicates that  $x_3$  always equals to  $x_4$ . Utilizing  $x_1$ ,  $x_2$ ,  $x_3$ , and the condition  $x_1 + x_2 + 2x_3 = n$ , the eigenvalue of  $H/J$  can be expressed by  $-[2+g(t)]x_1 + [-2+g(t)]x_2 + n$ . Hence, the calculation of the maximum eigenvalue is equivalent to a linear optimization problem: the maxi-

mization of  $-[2+g(t)]x_1 + [-2+g(t)]x_2 + n$  under some constraints on  $x_1$ ,  $x_2$ , and  $x_3$ . It is easy to see that the natural constraints on  $x_1$ ,  $x_2$ , and  $x_3$  are  $0 \leq x_1, x_2 \leq n$  and  $0 \leq x_3 \leq \lfloor n/2 \rfloor$ . Here  $\lfloor \cdot \rfloor$  is the floor function. Combing the equation  $x_1 + x_2 + 2x_3 = n$ , the condition  $0 \leq x_3 \leq \lfloor n/2 \rfloor$  is equivalent to  $0 \leq x_1 + x_2 \leq n$  when  $n$  is even and  $1 \leq x_1 + x_2 \leq n$  when  $n$  is odd, which can be unified as  $\frac{1}{2}[1+(-1)^{n+1}] \leq x_1 + x_2 \leq n$ . This condition is fully contained by the constraint  $0 \leq x_1, x_2 \leq n$ . Hence, the full linear optimization problem can be expressed by

$$\begin{aligned} & \max_{x_1, x_2} -[2+g(t)]x_1 + [-2+g(t)]x_2 + n, \\ & \text{subject to } \begin{cases} \eta \leq x_1 + x_2 \leq n, \\ x_1, x_2 \in \mathbb{N}. \end{cases} \end{aligned} \quad (\text{C41})$$

Here  $\eta := \frac{1}{2}[1+(-1)^{n+1}]$  and  $\mathbb{N}$  is the set of natural numbers.

To solve this problem, four cases have to be discussed: (1)  $g(t) \leq -2$ , (2)  $-2 < g(t) \leq 0$ , (3)  $0 < g(t) < 2$ , and (4)  $g(t) \geq 2$ . In the case that  $g(t) \leq -2$ , the coefficients  $-[2+g(t)] \geq 0$  and  $-2+g(t) \leq 0$ , indicating that the maximum eigenvalue is obtained when  $x_1$  is largest and  $x_2$  vanishes, i.e.,  $x_1 = n$ ,  $x_2 = 0$ . The corresponding maximum eigenvalue is  $n[-g(t) - 1]$ . In the case that  $g(t) \in (-2, 0]$ , both coefficients  $-[2+g(t)]$  and  $-2+g(t)$  are negative, and the maximum eigenvalue is attained by the lower bounds of  $x_1$  and  $x_2$ . If  $n$  is even, the minimum value of  $x_1$  and  $x_2$  are both zero, which leads to the maximum value  $n$ . If  $n$  is odd, the maximum value is attained by  $x_1 = 1$ ,  $x_2 = 0$  due to the fact that  $-[2+g(t)]$  is larger than  $-2+g(t)$ . The corresponding maximum value is  $n - 2 - g(t)$ . In the case that  $g(t) \in (0, 2)$ , the situation is similar to the second one. The maximum value is  $n$  and attained by  $x_1 = x_2 = 0$  when  $n$  is even. For an odd  $n$ , the maximum value is  $n - 2 + g(t)$ , which can be attained by  $x_1 = 0$ ,  $x_2 = 1$ . In the last case that  $g(t) \geq 2$ ,  $-[2+g(t)] \leq 0$  and  $-2+g(t) \geq 0$ . The maximum value is  $n[g(t) - 1]$ , which is attained by  $x_1 = 0$ ,  $x_2 = n$ . In summary, the maximum eigenvalue of  $H/J$  is of the form

$$E_{\max, p} = \begin{cases} n - \eta[2 - |g(t)|], & |g(t)| < 2, \\ n[|g(t)| - 1], & |g(t)| \geq 2. \end{cases} \quad (\text{C42})$$

Now we consider a specific case that  $g(t) = B \cos(\omega t)$ , where  $B$  is a positive amplitude and  $\omega$  is the frequency. The QOQS  $\tau$  is solved via the equation

$$\int_0^\tau E_{\max, p}(t) - E_{\min, p}(t) dt = \Theta. \quad (\text{C43})$$

When  $B < 2$ ,  $|g(t)|$  is always less than 2, which means  $E_{\max, p}$  always takes the form  $n - \eta[2 - |g(t)|]$ , and Eq. (C43) reduces to

$$2(n - \eta)\tau + (n + \eta) \int_0^\tau |g(t)| dt = \Theta. \quad (\text{C44})$$

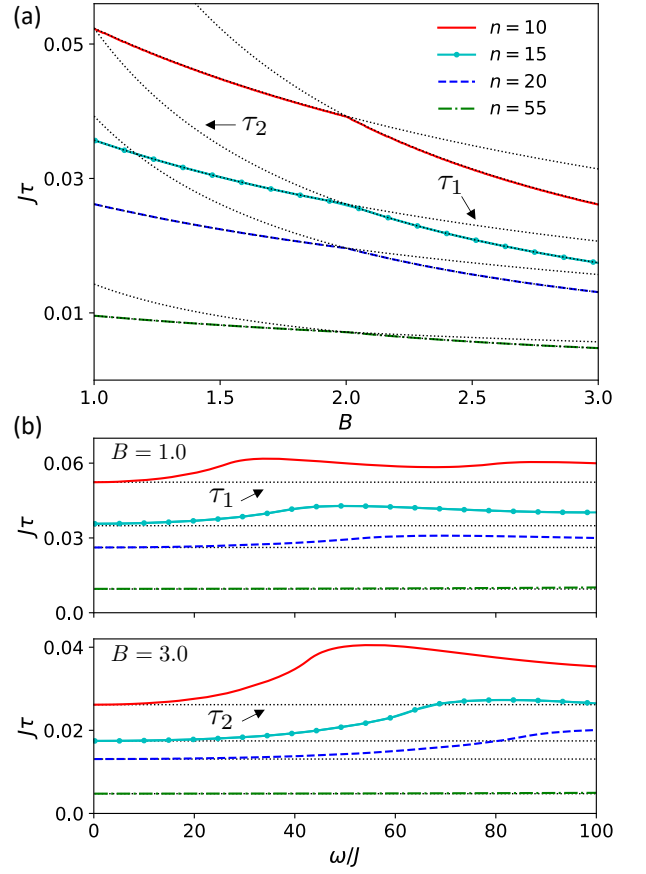


Figure 6. Validity of the approximation with the changes of (a) the amplitude  $B$  and (b) the frequency  $\omega$  for  $n = 10$  (solid red lines),  $n = 15$  (solid circle cyan lines),  $n = 20$  (dashed blue lines), and  $n = 55$  (dash-dotted green lines).  $\omega/J = 1$  in (a), and in (b)  $B = 1.0$  and  $B = 3.0$  for the upper and lower panels, respectively.

For a not very large  $\omega$ ,  $\int_0^\tau |g(t)| dt = \frac{B}{\omega} \sin(\omega\tau) \approx B\tau$ . Hence,

$$\tau \approx \frac{\Theta}{2(n - \eta) + B(n + \eta)} =: \tau_1. \quad (\text{C45})$$

When  $B > 2$ , the relation between  $|g(t)|$  and 2 is not fixed at different time. However, for a not very large  $\omega$ ,  $\tau$  is still very small in this case, which means  $E_{\max, p}$  takes the form  $n[g(t) - 1]$  before the time  $\tau$ , and  $\int_0^\tau |g(t)| dt$  still approximates to  $B\tau$ . Therefore, according to Eq. (C43),  $\tau$  approximates to

$$\tau \approx \frac{\Theta}{2Bn} =: \tau_2. \quad (\text{C46})$$

The validity of approximation is numerically tested with the changes of amplitude  $B$  and frequency  $\omega$  for different spin number  $n$ . As shown in Fig. 6(a), the performance of approximation is very well for different values of  $B$  when  $\omega$  is not extremely large [ $\omega/J = 1$  in the plot]. As to the frequency  $\omega$ , the approximation is valid when  $\omega$  is no larger than around 10 for both  $B = 1.0$  [upper

panel in Fig. 6(b)] and  $B = 3.0$  (lower panel). As a matter of fact,  $\tau_1$  and  $\tau_2$  are nothing but the OQSLs for the constant external field  $g(t) = B$ . Hence, the validity of approximation for a large regime of  $\omega$  indicates that the OQSL is way more sensitive to the amplitude than the frequency as long as the frequency is not extremely large.

*b. Open boundary condition*

Next we consider the case of the open boundary condition. The corresponding Hamiltonian reads

$$H/J = - \sum_{j=1}^{n-1} \sigma_j^z \sigma_{j+1}^z - \sum_{j=1}^n g(t) \sigma_j^z. \quad (\text{C47})$$

In this case, the minimum eigenvalue of  $-\sigma_j^z \sigma_{j+1}^z - g(t) \sigma_j^z$  is  $-1 - g(t)$  [ $-1 + g(t)$ ] for  $g(t) \geq 0$  [ $g(t) \leq 0$ ], which leads to the minimum eigenvalue of  $H/J$

$$E_{\min,o} = -n [1 + |g(t)|] + 1. \quad (\text{C48})$$

The minimum eigenvalue can be attained by the eigenstate  $|\uparrow\rangle^{\otimes n}$  [ $|\downarrow\rangle^{\otimes n}$ ] for  $g(t) \geq 0$  [ $g(t) < 0$ ].

To calculate the maximum eigenvalue, we rewrite the Hamiltonian into the form

$$H/J = H_p + \sigma_n^z \sigma_1^z, \quad (\text{C49})$$

where  $H_p$  is the Hamiltonian under the periodic boundary condition. Now let us denote  $E_{\max,p}$  and  $|E_{\max,p}\rangle$  as the maximum eigenvalue and corresponding eigenstate of  $H_p$ , which is actually already obtained in the previous discussion. Notice that the eigenstates of  $H_p$  are also eigenstates of  $\sigma_n^z \sigma_1^z$ , and the corresponding eigenvalues can only be 1 and  $-1$ . Hence, if  $|E_{\max,p}\rangle$  also corresponds to the eigenvalue 1, i.e.,  $\sigma_n^z \sigma_1^z |E_{\max,p}\rangle = |E_{\max,p}\rangle$ , then the maximum energy for the entire Hamiltonian is just  $E_{\max,p} + 1$ . As a matter of fact, this is just the case for any  $n$  in the regime  $|g(t)| \geq 2$ , and for odd  $n$  in the regime  $|g(t)| < 2$ . Hence, the maximum eigenvalue  $E_{\max}$  for these cases reads

$$E_{\max,o} = \begin{cases} n [|g(t)| - 1] + 1, & |g(t)| \geq 2, \\ n + |g(t)| - 1, & |g(t)| < 2 \text{ and } n \text{ is odd.} \end{cases}$$

For an even  $n$  in the regime  $|g(t)| < 2$ ,  $E_{\max,p} - 1 = n - 1$  may not be the maximum eigenvalue anymore. Another possible candidate must be among the eigenvalues of which the corresponding eigenstate  $|E_c\rangle$  satisfies  $\sigma_n^z \sigma_1^z |E_c\rangle = |E_c\rangle$ . It is obvious that we only need to find the maximum eigenvalues in this case and compare it with  $E_{\max,p} - 1$ . This maximization problem can still be formulated as a linear optimization problem as follows

$$\begin{aligned} & \max_{x_1, x_2} -[2 + g(t)]x_1 + [-2 + g(t)]x_2 + n + 1, \\ & \text{subject to } \begin{cases} 2 \leq x_1 + x_2 \leq n, \\ x_1, x_2 \in \mathbb{N}, \\ |g(t)| \leq 2. \end{cases} \end{aligned} \quad (\text{C50})$$

The constraint  $x_1 + x_2 \geq 2$  comes from the fact that  $\sigma_n^z \sigma_1^z |E_c\rangle = |E_c\rangle$  is equivalent to require  $x_1 \geq 1$  or  $x_2 \geq 1$ , and  $x_1 + x_2 + 2x_3 = n$  requires  $x_1 + x_2$  has to be an even number when  $n$  is even. Hence,  $x_1 + x_2$  has to be no smaller than 2. Since both the coefficients  $-[2 + g(t)]$  and  $-2 + g(t)$  are nonpositive in this case, the maximum value must be attained by  $x_1 = 2, x_2 = 0$  or  $x_1 = 0, x_2 = 2$ . Therefore, in this case the maximum eigenvalue is  $n + 2|g(t)| - 3$ . Next we need to compare the value between  $n - 1$  and  $n + 2|g(t)| - 3$ . As a matter of fact, it is easy to see when  $n - 1$  is larger when  $|g(t)| < 1$  and  $n + 2|g(t)| - 3$  is larger when  $|g(t)| > 1$ . In summary, the maximum eigenvalue  $E_{\max,o}$  under the open boundary condition reads

$$\begin{cases} n - 1, & |g(t)| \leq 1 \text{ and } n \text{ is even,} \\ n + 2|g(t)| - 3, & 1 < |g(t)| < 2 \text{ and } n \text{ is even,} \\ n + |g(t)| - 1, & |g(t)| < 2 \text{ and } n \text{ is odd,} \\ n [|g(t)| - 1] + 1, & |g(t)| \geq 2. \end{cases} \quad (\text{C51})$$

Utilizing the symbol  $\eta = [1 + (-1)^{n+1}]/2$ , the equation above can be rewritten into

$$E_{\max,o} = \begin{cases} n + \eta |g(t)| - 1, & |g(t)| \leq 1, \\ n - (2 - \eta)[2 - |g(t)|] + 1, & 1 < |g(t)| < 2, \\ n [|g(t)| - 1] + 1, & |g(t)| \geq 2. \end{cases} \quad (\text{C52})$$

Next we calculate the OQSL. In the case that  $|g(t)| \leq 1$ ,  $\tau$  satisfies the equation

$$(n + \eta) \int_0^\tau |g(t)| dt + (2n - 2)\tau = \Theta. \quad (\text{C53})$$

It is easy to see that here  $\int_0^\tau |g(t)| dt$  is less than  $\tau$ , indicating that

$$\tau \geq \frac{\Theta}{3n - 2 + \eta}. \quad (\text{C54})$$

When  $1 < |g(t)| < 2$ ,  $\tau$  satisfies

$$(n + 2 - \eta) \int_0^\tau |g(t)| dt + (2n - 4 + 2\eta)\tau = \Theta, \quad (\text{C55})$$

which gives

$$\frac{\Theta}{4n} < \tau < \frac{\Theta}{3n - 2 + \eta} \quad (\text{C56})$$

due to the fact that  $\tau < \int_0^\tau |g(t)| dt < 2\tau$ . When  $|g(t)| \geq 2$ , the OQSL satisfies

$$2n \int_0^\tau |g(t)| dt = \Theta, \quad (\text{C57})$$

which means  $\tau \leq \Theta/(4n)$ .

Let us still consider a specific form of  $g(t)$  that  $g(t) = B \cos(\omega t)$ . Similar to the case with the periodic boundary condition, the approximated expressions of OQSL can

also be analytically obtained utilizing the approximation  $\int_0^\tau |g(t)|dt \approx B\tau$  for a not very large  $\omega$ . In the regime  $B \geq 2$ , the OQSL is the same with  $\tau_2$  [Eq. (C46)]. A more interesting phenomenon occurs in the regime  $B < 2$ , where the OQSL is different from  $\tau_1$  [Eq. (C45)] for an even  $n$ . Specifically, the OQSL is

$$\tau \approx \frac{\Theta}{nB + 2n - 2} =: \tau_3 \quad (\text{C58})$$

when  $B \leq 1$ , and it is

$$\tau \approx \frac{\Theta}{nB + 2n + 2B - 4} \quad (\text{C59})$$

when  $1 < B < 2$ . The maximum gap between the OQSLs for periodic and open boundary conditions happens at the point  $B = 0$ , i.e., when no external field exists. In this case, the OQSL can be rigorously solved and the difference is

$$\tau_3 - \tau_1 = \frac{\Theta}{2n(n-1)} =: \Delta\tau. \quad (\text{C60})$$

The optimal states to realize  $\tau_1$  and  $\tau_3$  are in the form of Eq. (C13). One thing that should be noticed is that the dimension of  $\xi$  in the case of periodic boundary condition could be different from that in the case of the open boundary condition due to the different degeneracy of minimum and maximum energies in these two cases.

### c. Robustness analysis

The dependence on the boundary condition indicates that the OQSL may be used to detect whether an even-numbered spin ring is ruptured. To do that, one needs to prepare the optimal states in Eq. (C12) and then measure  $\text{Tr}(\rho_0\rho_t)$  and  $\text{Tr}(\rho_t^2)$  at time  $\tau_3$  and  $\tau_1$ , which can be realized via techniques like randomized measurements [58, 59]. Here  $\rho_0$  and  $\rho_t$  are the initial state and evolved state at time  $t$ . After the measurement, the Bloch angle can be calculated via the equation

$$\cos(\theta(t)) = \frac{\text{Tr}(\rho_0\rho_t) - 2^{-n}}{\sqrt{[\text{Tr}(\rho_0^2) - 2^{-n}][\text{Tr}(\rho_t^2) - 2^{-n}]}}. \quad (\text{C61})$$

If the target is fulfilled at time  $\tau_3$ , then the ring is ruptured, and it is complete if the target is fulfilled at the time  $\tau_1$ .

A more interesting fact is that the evolution time for the states in Eq. (C12) is robust to the global and local dephasing. The global dephasing is described by the master equation

$$\partial_t \rho_t = -i[H, \rho_t] + \gamma_g \left( J_z \rho_t J_z - \frac{1}{2} \{ \rho_t, J_z^2 \} \right) \quad (\text{C62})$$

with  $\gamma_g$  the decay rate and  $J_z = \frac{1}{2} \sum_{j=1}^n \sigma_j^z$ , and the local dephasing is described by

$$\partial_t \rho_t = -i[H, \rho_t] + \sum_{j=1}^n \gamma_{l,j} (\sigma_j^z \rho_t \sigma_j^z - \rho_t), \quad (\text{C63})$$

where  $\gamma_{l,j}$  is the decay rate for  $j$ th spin.

Now we analytically discuss this robustness under global and local dephasing. We need to emphasize that the optimal states [Eq. (C12)] in the noiseless case may not keep optimal when global and local dephasing are involved, and the corresponding evolution time to reach the target may also not be the OQSL anymore. The analysis of OQSL under the noise requires the CRC methodology. Here we only discuss the robustness of the evolution time for the states in Eq. (C12).

Recall that the states in Eq. (C12) can be written into Eq. (C13) in the basis  $\{|E_0\rangle, |E_1\rangle, \dots, |E_{2^n-1}\rangle\}$ . Without the external field, the degeneracy of ground states and the highest energy levels are both two. In the meantime, due to the fact that  $\sigma_j^z$  (for any  $j$ ) and  $J_z$  are both diagonal in this basis, we are allowed to denote  $J_z = \text{diag}(A, \dots, G)$  with  $A$  and  $G$  2-dimensional diagonal matrices, and  $\sigma_j^z = \text{diag}(C_j, \dots, D_j)$  with  $C_j$  and  $D_j$  2-dimensional diagonal matrices. Utilizing these notations, the master equation for global dephasing [Eq. (C62)] reduces to the evolution of the block  $\xi$  as follows

$$\partial_t \xi_t = i(E_{\max} - E_{\min})\xi_t + \gamma_g A \xi_t G - \frac{\gamma_g}{2} (\xi_t G^2 + A^2 \xi_t), \quad (\text{C64})$$

where  $\xi_t$  is the evolved block at time  $t$ , and the one for local dephasing [Eq. (C63)] reduces to

$$\partial_t \xi_t = i(E_{\max} - E_{\min})\xi_t + \sum_j \gamma_{l,j} (C_j \xi_t D_j - \xi_t). \quad (\text{C65})$$

As long as the specific forms of  $A$ ,  $G$ ,  $C_j$ , and  $D_j$  are known, the dynamics can be easily solved. Next, we show the calculations of these blocks.

It is not difficult to see that  $\sigma_j^z$  is easy to be expressed in the basis  $\{|\uparrow\rangle, |\downarrow\rangle\}^{\otimes n}$ , and the specific forms of  $\sigma_j^z$  (diagonal values) for different values of  $j$  are shown in Fig. 7(a), where  $\vec{1}_k$  ( $-\vec{1}_k$ ) represents a  $k$ -dimensional vector with all entries 1 ( $-1$ ). To find the expressions of  $C_j$  and  $D_j$ , we need to know the entry positions of minimum and maximum energies for the Hamiltonian  $-\sum_j \sigma_j^z \sigma_{j+1}^z$  and extract the values of  $\sigma_j^z$  in the same positions to reconstruct  $C_j$  and  $D_j$ . The expression of  $-\sigma_j^z \sigma_{j+1}^z$  in the basis  $\{|\uparrow\rangle, |\downarrow\rangle\}^{\otimes n}$  for different values of  $j$  are given in Fig. 7(b). In this diagram, searching the entry positions of the minimum and maximum energies is equivalent to searching a column with the most number of  $-1$  and  $1$ . It can be seen that the entries of  $-\sigma_j^z \sigma_{j+1}^z$  for all values of  $j$  are symmetric, indicating that the entire diagram can be divided into four blocks, where the first and fourth (second and third) blocks are mirror symmetric. The positions with respect to the minimum energy are easy to locate since only the first and last entries of  $-\sigma_j^z \sigma_{j+1}^z$  are always  $-1$  for all values of  $j$ . Hence, their summation (summation of the column in dashed-red boxes) would also be the minimum. In the meantime, the first and last entries of  $\sigma_j^z$  are always  $1$  and  $-1$  for all values of  $j$ , indicating that  $C_j = \sigma_z$ . Moreover, due to the fact that  $J_z$  is half of the summation of all  $\sigma_j^z$ , the entry positions in  $J_z$  that



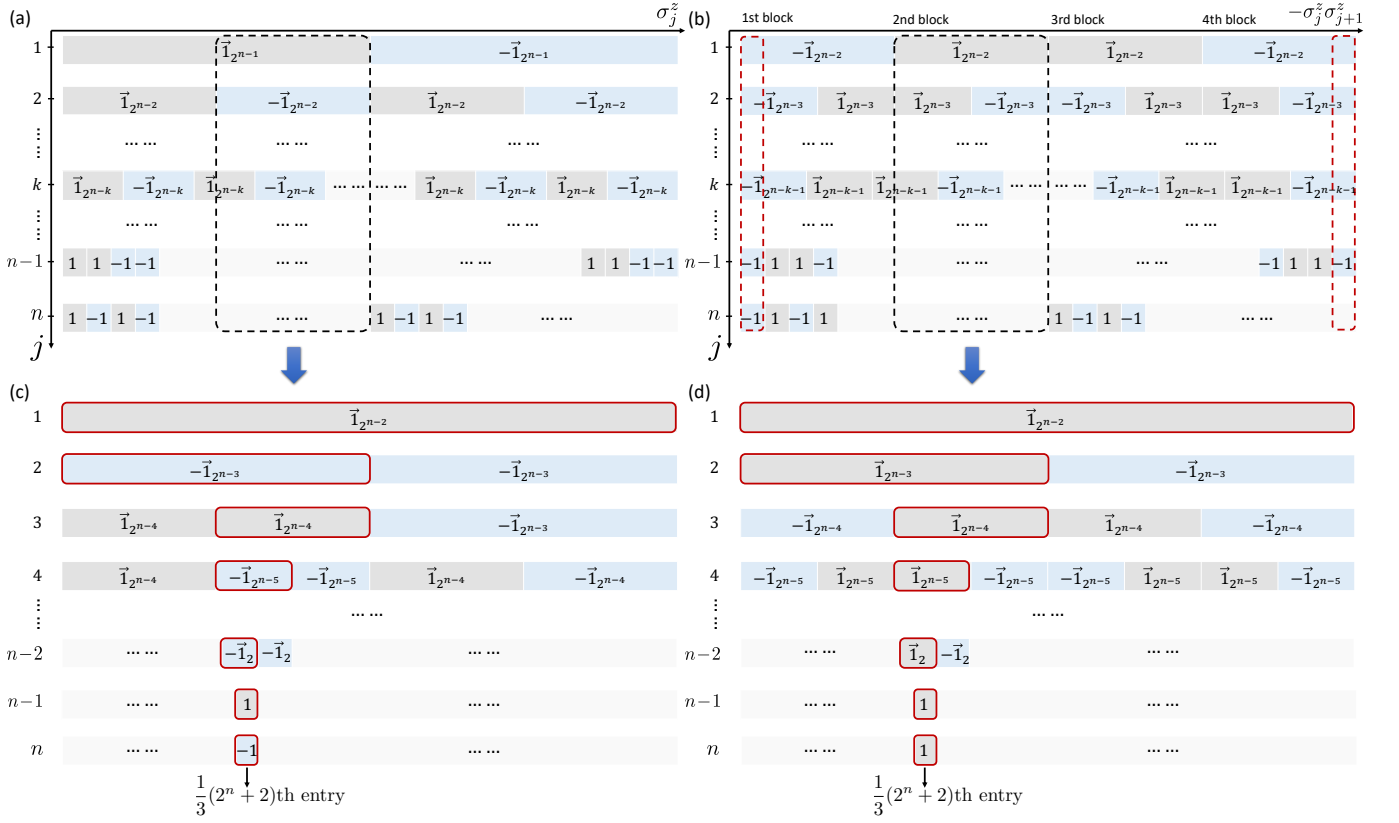


Figure 7. Schematic for the search of entry positions of the minimum and maximum energies. (a) The diagonal entry distribution for  $\sigma_j^z$ ; (b) The diagonal entry distribution for  $-\sigma_j^z \sigma_{j+1}^z$ . [(c),(d)] The second blocks for  $\sigma_j^z$  and  $-\sigma_j^z \sigma_{j+1}^z$  for the search of the maximum energy.

correspond to the minimum energy are also the first and last entries, which means  $A = \text{diag}(n/2, -n/2) = n\sigma_z/2$ .

For the sake of finding the entry positions of the maximum energy, we need to locate the position where the entry is always 1 for any value of  $j$ , namely, a column in the diagram where all entries are 1. It is obvious that it can only exist in the second and third blocks. Due to the symmetry, we only need to consider the second block. As shown in Fig. 7(d), a significant feature in this block is that the overlap between the positions of  $\vec{1}$  in the  $j$ th and  $(j+1)$ th lines halves. More specifically to say, compared to the position of  $\vec{1}$  in the  $j$ th line, only the left (right) half in the same position keeps being 1 in the  $(j+1)$ th line if  $j$  is odd (even). For example, in the first line ( $j=1$ ) all entries are 1, and hence the length of  $\vec{1}$  is  $2^{n-2}$ . In the second line ( $j=2$ ), only the left half keeps being one, and the length of  $\vec{1}$  becomes  $2^{n-3}$ . Similarly, in the third line ( $j=3$ ) only the right half keeps being 1 compared to the position of  $\vec{1}$  in the second line. Utilizing this feature, one can find that when  $n$  is even, the  $\frac{1}{3}(2^n - 1)$ th and  $\frac{1}{3}(2^n + 2)$ th entries keep being 1 in the  $(n-2)$ th line. Notice that the entry number here starts from the beginning of all diagonal entries of  $-\sigma_j^z \sigma_{j+1}^z$ , not the beginning of the second block. And in the  $(n-1)$ th line, the  $\frac{1}{3}(2^n + 2)$ th entry is 1. In

the case of open boundary condition, this is the last line and the position is located. In the case of the periodic boundary condition, one more line of  $-\sigma_n^z \sigma_1^z$  needs to be considered. Luckily, this position of  $-\sigma_n^z \sigma_1^z$  is also 1 when  $n$  is even. Therefore, the maximum energy is at the  $\frac{1}{3}(2^n + 2)$ th entry under both boundary conditions. Due to the symmetry, the  $\frac{1}{3}(2^{n+1} + 1)$ th entry, which is in the third block, is also maximum.

Now we locate the values of  $\frac{1}{3}(2^n + 2)$ th and  $\frac{1}{3}(2^{n+1} + 1)$ th entries in  $\sigma_j^z$ , which is irrelevant to the boundary condition. The block of entries in  $\sigma_j^z$  with respect to the second block in Fig. 7(b) is given in Fig. 7(c). As shown in this diagram, the  $\frac{1}{3}(2^n + 2)$ th entry is 1 for an odd  $j$  and  $-1$  for an even  $j$ , namely, it is  $(-1)^{j+1}$ . Similarly, one can find that the  $\frac{1}{3}(2^{n+1} + 1)$ th entry is  $(-1)^j$ . Hence,  $D_j = (-1)^{j+1} \sigma_z$ . In the meantime, both  $\frac{1}{3}(2^n + 2)$ th and  $\frac{1}{3}(2^{n+1} + 1)$ th entries are zero in  $J_z$  when  $n$  is even, which means  $G = 0$ .

In summary, we have found that  $A = n\sigma_z/2$ ,  $G = 0$ ,  $C_j = \sigma_z$ , and  $D_j = (-1)^{j+1} \sigma_z$ . Utilizing these expressions, Eqs. (C64) and (C65) can be further written into

$$\partial_t \xi_t = \left[ i(E_{\max} - E_{\min}) - \frac{n^2 \gamma g}{8} \right] \xi_t, \quad (\text{C66})$$

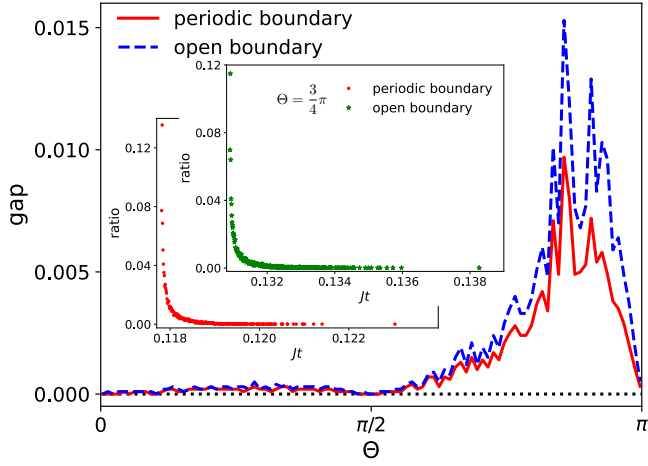


Figure 8. The variety of the gap between the maximum and minimum values of the evolution time to reach the target  $\Theta$  among 100 random states with random values of  $\{\gamma_{l,j}\} \in (0, 1)$ . The insets present the ratios of 10000 states at different evolution time to reach the target  $\Theta = 3\pi/4$  for periodic (red dots) and open (green pentagrams) boundary conditions.  $n = 10$  in all plots.

and

$$\partial_t \xi_t = i(E_{\max} - E_{\min})\xi_t + \sum_j \gamma_{l,j} [(-1)^{j+1} \sigma_z \xi_t \sigma_z - \xi_t]. \quad (\text{C67})$$

Equation (C66) can be easily solved as

$$\xi_t = e^{\left[ i(E_{\max} - E_{\min}) - \frac{n^2 \gamma_g}{8} \right]} \xi, \quad (\text{C68})$$

and Eq. (C67) can be solved as

$$\begin{aligned} [\xi_t]_{00(11)} &= e^{i(E_{\max} - E_{\min}) - \sum_{j=1}^n \gamma_{l,j} [1 + (-1)^j]} [\xi]_{00(11)}, \\ [\xi_t]_{01(10)} &= e^{i(E_{\max} - E_{\min}) - \sum_{j=1}^n \gamma_{l,j} [1 - (-1)^j]} [\xi]_{01(10)}. \end{aligned}$$

Here  $[\cdot]_{ab}$  represents the  $ab$ th entry ( $a, b = 0, 1$ ).

Next we calculate  $\cos(\theta(t))$ . Notice that Eq. (C61) can be expressed by

$$\cos(\theta(t)) = \frac{\text{Re} \left( \text{Tr}(\xi \xi_t^\dagger) \right)}{\sqrt{\text{Re}(\text{Tr}(\xi \xi^\dagger)) \text{Re}(\text{Tr}(\xi_t \xi_t^\dagger))}}, \quad (\text{C69})$$

where  $\text{Re}(\cdot)$  represents the real part. In the case of global dephasing [Eq. (C66)], the expression above reduces to

$$\cos(\theta(t)) = \cos((E_{\max} - E_{\min})t), \quad (\text{C70})$$

which is irrelevant to the decay rate  $\gamma$ . Hence, the evolution time to reach the target for the optimal states in Eq. (C13) is indeed robust to the global dephasing in both periodic and open boundary conditions, indicating that their difference is also robust.

In the case of local dephasing, Eq. (C69) can be expressed by

$$\begin{aligned} & \cos(\theta(t)) \\ &= \cos((E_{\max} - E_{\min})t) \frac{\varsigma_1 + \varsigma_2 e^{-2t\gamma_{\text{all}}}}{\sqrt{\varsigma_1 + \varsigma_2} \sqrt{\varsigma_1 + \varsigma_2 e^{-4t\gamma_{\text{all}}}}}, \end{aligned}$$

where  $\varsigma_1 = |[\xi_t]_{00}|^2 + |[\xi_t]_{11}|^2$ ,  $\varsigma_2 = |[\xi_t]_{01}|^2 + |[\xi_t]_{10}|^2$ , and  $\gamma_{\text{all}} = \sum_{j=1}^n \gamma_{l,j} (-1)^j$ . If the values of all decay rates  $\{\gamma_{l,j}\}$  are very close, for example  $\gamma_{l,j} \approx \gamma$  for any  $j$ , then  $\gamma_{\text{all}} \approx 0$  and  $\cos(\theta(t))$  still approximates to  $\cos((E_{\max} - E_{\min})t)$ , which is also irrelevant to the decay rates, and thus in this case the evolution time, as well as the time difference, are also robust to the local dephasing. In the case that the values of  $\{\gamma_{l,j}\}$  are not close, Eq. (C69) is indeed dependent on the decay rates. However, since  $\varsigma_1 + \varsigma_2 e^{-2t\gamma_{\text{all}}}$  is always positive at finite time, the evolution time is still irrelevant to  $\gamma_{\text{all}}$  for the target  $\Theta = \pi/2$  and hence robust to the local dephasing. For a general target, we have tested 100 random states in Eq. (C13) with random values of  $\{\gamma_{l,j}\} \in (0, 1)$  for each target in the case of  $n = 10$ , and the gap between the maximum and minimum values of the evolution time for these 100 states are given in Fig. 8. It can be seen that the robustness is quite good when the target is no larger than  $\pi/2$ , and it is indeed compromised when  $\Theta$  is larger than  $\pi/2$ . Even for those targets with large gaps, the evolution time for different states could concentrate on some specific values, namely, the distribution of states in the gap has a sharp peak. For example, the insets of Fig. 8 show the distributions of 10000 states for periodic (red dots) and open (green pentagrams) boundary conditions in the case of  $\Theta = 3\pi/4$ . It can be seen that the distributions for both periodic and open boundary conditions have a sharp peak at the minimum values, indicating that the evolution time is still relatively robust for most states.

## Appendix D: Learning the OQSL in Landau-Zener model

### 1. Verification of the validity of CRC methodology

Here we present the process of learning the OQSL in the Landau-Zener model and show the validity of the CRC methodology. The Hamiltonian of this model is

$$H = \Delta \sigma_x + v t \sigma_z, \quad (\text{D1})$$

where  $\Delta$  and  $v$  are two time-independent parameters.  $\sigma_x$  and  $\sigma_z$  are the Pauli matrices. The OQSL in this model has been thoroughly discussed in Ref. [21], in which the set  $\mathcal{S}$  is obtained via the brute-force search among around one million pure states. The reason why only pure states are considered here is due to the fact that unitary evolution does not affect the purity and in the Bloch representation all states in the same direction can/cannot

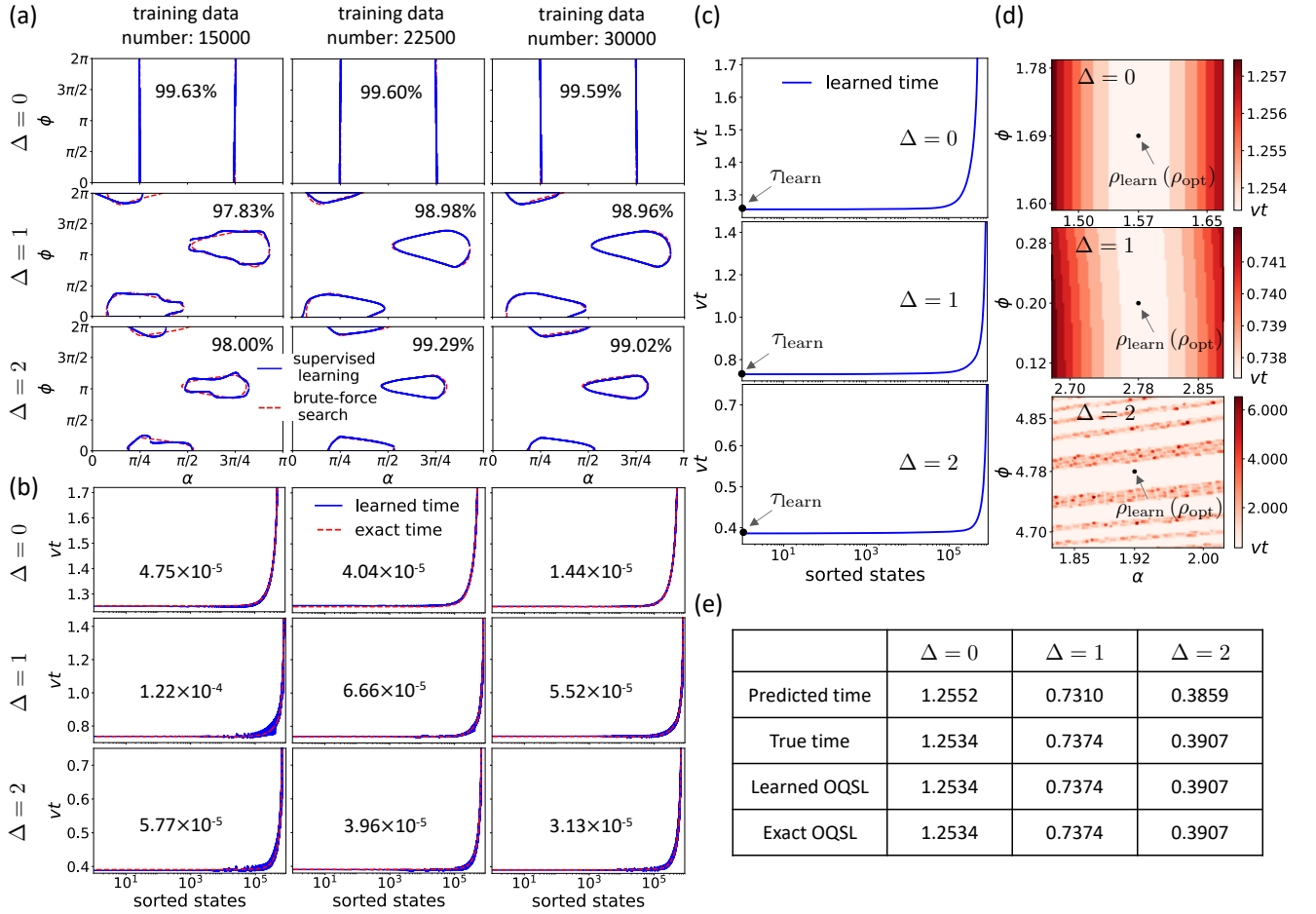


Figure 9. (a) Comparison between the set  $\mathcal{S}$  (brute-force search) and  $\mathcal{S}_{\text{learn}}$  (learning) with different values of  $\Delta$  and different training data number. The first, second, and third rows represent the results for  $\Delta = 0$ ,  $\Delta = 1$ , and  $\Delta = 2$ , respectively. The first, second, and third columns represent the results for 15000, 22500, and 30000 training data, respectively. The solid blue (dashed red) lines represent the boundaries between  $\mathcal{S}$  ( $\mathcal{S}_{\text{learn}}$ ) and its complementary set. The percentage numbers in the plots are the scores of the learning. (b) Comparison of the evolution time to reach the target obtained from the regression process (solid blue lines) and the exact time obtained from the brute-force search (dashed red lines). Here the input states in the regression are the ones in  $\mathcal{S}$ . The numbers in the plots are the mean square errors of learning. (c) The practical performance of the regression process where the input states are those in  $\mathcal{S}_{\text{learn}}$ . (d) Results of the calibration process. The region for calibration is taken as  $[\alpha_{\text{learn}} - 0.1, \alpha_{\text{learn}} + 0.1]$  and  $[\phi_{\text{learn}} - 0.1, \phi_{\text{learn}} + 0.1]$ . The black dots represent  $(\alpha_{\text{learn}}, \phi_{\text{learn}})$ , the "optimal" points obtained in the regression. (e) Table of the predicted time ( $\tau_{\text{learn}}$ ) obtained in the practical regression process, the corresponding true time, and finally learned OQSL after the calibration process for different values of  $\Delta$ . The exact OQSL is obtained via brute-force search. In all plots  $v$  is set to be 1 and the target angle  $\Theta = \pi/2$ .

reach the target simultaneously. The dynamics is solved via QuTiP [60, 62]. The full evolution is truncated at  $vt = 10$ , namely, the state is treated to not be in  $\mathcal{S}$  if it cannot reach the target within the truncated time. The Bloch vector of the initial state is parameterized by  $\vec{r} = (\sin \alpha \cos \phi, \sin \alpha \sin \phi, \cos \alpha)^T$  with  $\alpha \in [0, \pi]$  and  $\phi \in [0, 2\pi)$ .

In the step of classification, a multilayer neural network with two inputs ( $\alpha$  and  $\phi$ ) and one output (1 or 0) is created with a hyperbolic tangent function as the activation function. The output result 1/0 represents that the input initial state can/cannot realize the given target, respectively. Supervised learning is performed via

scikit-learn [61]. The network contains five to six hidden layers each with about 200 to 250 neurons. The Cross-Entropy loss function [64] is used as the loss function, and Adam [65] is applied in the updates of the network. The test set contains all the initial states (around one million states) used in the brute-force search. The performance of training for different values of  $\Delta$  are given in Fig. 9(a). The first, second, and third rows represent the learned  $\mathcal{S}$  for  $\Delta = 0$ ,  $\Delta = 1$ , and  $\Delta = 2$  (in the units of  $\sqrt{v}$ ). The solid blue and dashed red lines represent the boundaries between  $\mathcal{S}$  and its complementary set obtained via supervised learning and brute-force search. Different numbers of the training set, including 15000,

22500, and 30000, have also been tested and compared, as shown in the first (15000), second (22500), and third (30000) columns in Fig. 9(a). The percentage numbers in the plots are the scores of learning, i.e., the correctness of the network's output. It can be seen that the performance of 15000 training data is better than the others in the case of  $\Delta = 0$ , and 22500 training data present the best performance in the cases of  $\Delta = 1$  and  $\Delta = 2$ . One should notice that all the parameters of the network are manually tuned case by case, and the slight difference in the performance may not be fully due to the difference in the training data number. In the case of 22500 training data, the correctness is around 99%, indicating that about 0.99 million states are correctly classified into  $\mathcal{S}$  and its complementary set. Therefore, the neural network indeed works for the classification in this example.

The second step is the regression process, in which basically the same neural network is created but with rectified linear unit function as the activation function. The loss function is taken as the square error loss function [66]. The training data are sorted by the evolution time to reach the target from smallest to largest. Similar to the classification process, all the states in  $\mathcal{S}$  are used to test the performance of the network. Notice that  $\mathcal{S}$  here is the exact reachable state set obtained via the brute-force search since we need to check the validity of the network. The performance of regression is presented for different values of  $\Delta$  and training data number in Fig. 9(b). All the plots in this figure are semi-logarithmic ( $x$  axis). The first, second, and third rows represent the results for  $\Delta = 0$ ,  $\Delta = 1$ , and  $\Delta = 2$ . The first, second, and third columns represent the results for 15000, 22500, and 30000 training data. The number in the plots are the mean square errors of learning, i.e.,  $\frac{1}{m} \sum_{i=1}^m [t_{\text{pre}}^{(i)} - t_{\text{ext}}^{(i)}]^2$ . Here  $t_{\text{pre}}^{(i)}$  and  $t_{\text{ext}}^{(i)}$  are the predicted time obtained via learning and exact time obtained via brute-force search for the  $i$ th state. The order of states in the figure is sorted by the evolution time obtained in the brute-force search from smallest to largest, and the learned time is plotted using the same order of states. Notice that these states are not exactly the same for different values of  $\Delta$  due to the dependence of  $\mathcal{S}$  on  $\Delta$ . It can be seen that the performance of learning (solid blue lines) is good for all values of  $\Delta$ , especially when the training data number is 22500 and 30000. Basically the mean square errors of learning in these two cases for all values of  $\Delta$  are in the scale of  $10^{-5}$ . Hence, the network also works for the regression in this example.

As a matter of fact, in practice the reachable state set used in the regression process is the one obtained in the classification process (denoted by  $\mathcal{S}_{\text{learn}}$ ). Hence, although it is reasonable to use the true  $\mathcal{S}$  to check the validity of the regression,  $\mathcal{S}_{\text{learn}}$  has to be applied to test if the OQSL obtained from CRC methodology is reasonable. The performance of regression with respect to  $\mathcal{S}_{\text{learn}}$  for 22500 training data is given in Fig. 9(c) for different values of  $\Delta$ . The results for the other two training data numbers are not shown here due to their similar-

ity. Since the training set chosen in Fig. 9(b) is also a subset of  $\mathcal{S}_{\text{learn}}$ , we can directly use it as the training set in this case and the trained network is then the same. The states in the plots are sorted by the evolution time to reach the target from smallest to largest. As shown in this figure, the trend of learned time basically coincides with the exact time in Fig. 9(b). One should notice that in fact these two lines cannot be compared directly as the states are not exactly the same. Utilizing the result of the regression, the "optimal" state  $\rho_{\text{learn}}$  and corresponding predicted time  $\tau_{\text{learn}}$  can be located. The rigorous evolution time of  $\rho_{\text{learn}}$  to reach the target (true time) is given in the table in Fig. 9(e). It can be seen that the predicted time  $\tau_{\text{learn}}$  is very close to the true time for all values of  $\Delta$ . The errors in all cases are on the scale of  $10^{-3}$ , indicating that the regression process works well in this example. Furthermore, the true time of  $\rho_{\text{learn}}$  coincides with the exact OQSL obtained via brute-force search, which means  $\rho_{\text{learn}}$  is indeed an optimal state in this case.

The last process is calibration. The core of this process is to calculate the rigorous dynamics of the states around  $\rho_{\text{learn}}$  and find the exact minimum time in this region. This process guarantees the finally obtained time is the rigorous minimum time in this region. In this example, the values of  $(\alpha, \phi)$  for the "optimal" states [denoted by  $(\alpha_{\text{learn}}, \phi_{\text{learn}})$ ] in the cases of  $\Delta = 0$ ,  $\Delta = 1$ , and  $\Delta = 2$  are (1.57, 1.69), (2, 78, 0.20), and (1.92, 4.78), respectively [black dots in Fig. 9(d)]. The region to perform the calibration is  $[\alpha_{\text{learn}} - 0.1, \alpha_{\text{learn}} + 0.1]$  and  $[\phi_{\text{learn}} - 0.1, \phi_{\text{learn}} + 0.1]$ . The rigorous dynamics of about 10000 states in this region are calculated. The results are given in Fig. 9(d) and the corresponding minimum time (learned OQSL) is given in the table in Fig. 9(e). The consistency between the learned OQSL and the exact OQSL proves that the final result is indeed the exact OQSL in this example. The validity of the CRC methodology is then confirmed.

## 2. Learning the OQSL in the controlled system

Next, we apply the CRC methodology to search the OQSL in the controlled Landau-Zener model. The full Hamiltonian of this model reads

$$H = \Delta\sigma_x + vt\sigma_z + \vec{u} \cdot \vec{\sigma}, \quad (\text{D2})$$

where  $\vec{\sigma} = (\sigma_x, \sigma_y, \sigma_z)$  is the vector of Pauli matrices, and  $\vec{u} = (u_x, u_y, u_z)$  is the vector of control amplitudes.

We first discuss the generation of controls for a specific initial state to reach the target at the minimum time. The controls are generated via the auto-GRAPe [67] with the objective function

$$f = \int_0^T \cos(\theta(t)) dt, \quad (\text{D3})$$

where  $T$  is a reasonably long time (truncated time in our calculation), and  $\theta(t)$  is the angle between the Bloch vec-

---

**Algorithm 1:** auto-GRAPE
 

---

Initialize the control amplitude  $u_k(t)$  for all  $t$  and  $k$ ;  
**for** episode=1,  $M$  **do**  
 Receive initial state  $\rho_0$ ;  
**for**  $t = 1, T$  **do**  
 Evolve with the control  $\rho_t = e^{\Delta t \mathcal{L}_t} \rho_{t-1}$ ;  
 Calculate  $f_t = \frac{N\text{Tr}(\rho_0 \rho_t) - 1}{\sqrt{[N\text{Tr}(\rho_0^2) - 1][N\text{Tr}(\rho_t^2) - 1]}}$  and  
 save it;  
**end for**  
 Calculate the objective function  $f = \sum_t f_t$ .  
 Calculate the gradient  $\frac{\delta f}{\delta u_k(t)}$  with the automatic  
 differentiation method for all  $t$  and  $k$ .  
**for**  $t = 1, T$  **do**  
**for**  $k = 1, K$  **do**  
 Update control  $u_k(t) \leftarrow u_k(t) + \epsilon \frac{\delta f}{\delta u_k(t)}$ .  
**end for**  
**end for**  
**end for**  
 Save the controls  $\{u_k\}$ .

---

tors of initial state  $\rho_0$  and its evolved state  $\rho_t$ , which satisfies the equation  $\partial_t \rho_t = \mathcal{L}_t \rho_t$  with  $\mathcal{L}_t$  a time-dependent superoperator. Notice that in the Bloch representation the density matrix can be expressed by Eq. (A2). Then  $\cos(\theta(t))$  can be calculated by

$$\cos(\theta(t)) = \frac{N\text{Tr}(\rho_0 \rho_t) - 1}{\sqrt{[N\text{Tr}(\rho_0^2) - 1][N\text{Tr}(\rho_t^2) - 1]}}. \quad (\text{D4})$$

In this case, the dynamics is unitary and only pure states need to be calculated, then  $\cos(\theta(t))$  reduces to  $2\text{Tr}(\rho_0 \rho_t) - 1$ . In the numerical calculation, the evolution time is usually discretized into many equally spaced time points ( $\{t_i\}$ ), and thus we can use the discrete form

$$f = \sum_i \cos(\theta(t_i)) \quad (\text{D5})$$

as the objective function instead. The time interval here is neglected since it does not affect the final performance. In the numerical calculation, the difference between the discretization error of the integration and the value of the objective function is at the scaling of  $10^{-8}$  and thus this error would not cause any significant effect on the final result.

Auto-GRAPE is a gradient-based algorithm where the gradient is evaluated via automatic differentiation [67]. In Ref. [67] the quantum metrological quantities like quantum Fisher information are taken as the objective function, here in this paper we take Eq. (D5) as the objective function. The corresponding pseudocode is given in Algorithm 1. In one episode, the initial state is evolved to time  $T$  and the objective function is calculated. Then the gradients  $\delta f / \delta u_k(t)$  for all  $t$  and  $k$  are evaluated via automatic differentiation, which is realized with the Julia package Zygote [68]. At last, all the control amplitudes are updated simultaneously according to the evaluation

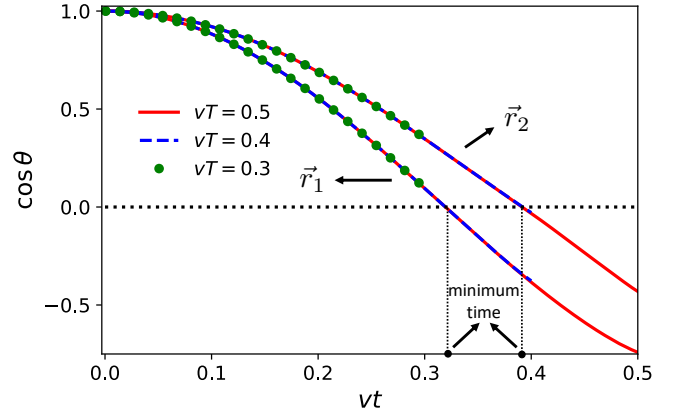


Figure 10. Performance of controls for two randomly generated initial states  $\vec{r}_1$  and  $\vec{r}_2$  with different values of  $T$  (in the unit of  $v$ ), including  $T = 0.3$  (green dots),  $T = 0.4$  (dashed blue lines), and  $T = 0.5$  (solid red lines).

of gradients. In practice, Adam [65] could be applied to further improve efficiency.

To test the validity of the objective function [Eq. (D5)], the performance of corresponding controls are demonstrated in Fig. 10 for two randomly generated initial states, of which the Bloch vectors are  $(0.22, 0.20, -0.96)^T := \vec{r}_1$  and  $(0.95, -0.15, -0.29)^T := \vec{r}_2$ . Three different values of  $T$  (in the unit of  $v$ ), including  $T = 0.3$  (green dots),  $T = 0.4$  (dashed blue lines), and  $T = 0.5$  (solid red lines) are tested. As shown in the figure, the optimal controls for  $T = 0.4$  and  $T = 0.5$  can let the states reach the target angle (dotted black line) at the same time, confirming that this found time (black dots) is indeed minimum. In the meantime, if  $T$  is smaller than the minimum time, for example  $T = 0.3$ , the states cannot reach the target angle during the entire evolution, which also corroborates that the found time is minimum as the states cannot reach the target before this time. Hence, the validity of the objective function and corresponding controls are confirmed. Moreover, the consistency of performance for  $T = 0.4$  and  $T = 0.5$  shows that the choice of  $T$  does not affect the result of minimum time as long as it is larger than the minimum time.

Next, we perform the CRC methodology for  $\Delta = 0, 1, 2, 3, 4, 5, 6$  (in the units of  $\sqrt{v}$ ) in both noiseless and noisy cases. In the noiseless case, the result of classification shows that all states in the state space can fulfill the target. This phenomenon is reasonable in physics due to the full controllability of  $\vec{u} \cdot \vec{\sigma}$ , which means the controls can realize the rotation of a state from any angle. Thus, any state can fulfill the target in finite time under this control Hamiltonian even without the free Hamiltonian  $\Delta \sigma_x + vt \sigma_z$ .

In the step of regression, the data number of training and test sets are 22500 and 7500. Similar to the noncontrolled case, the mean square errors between the learned time (solid blue lines) and exact time (dashed red lines) in the test set are still on the scales of  $10^{-5}$

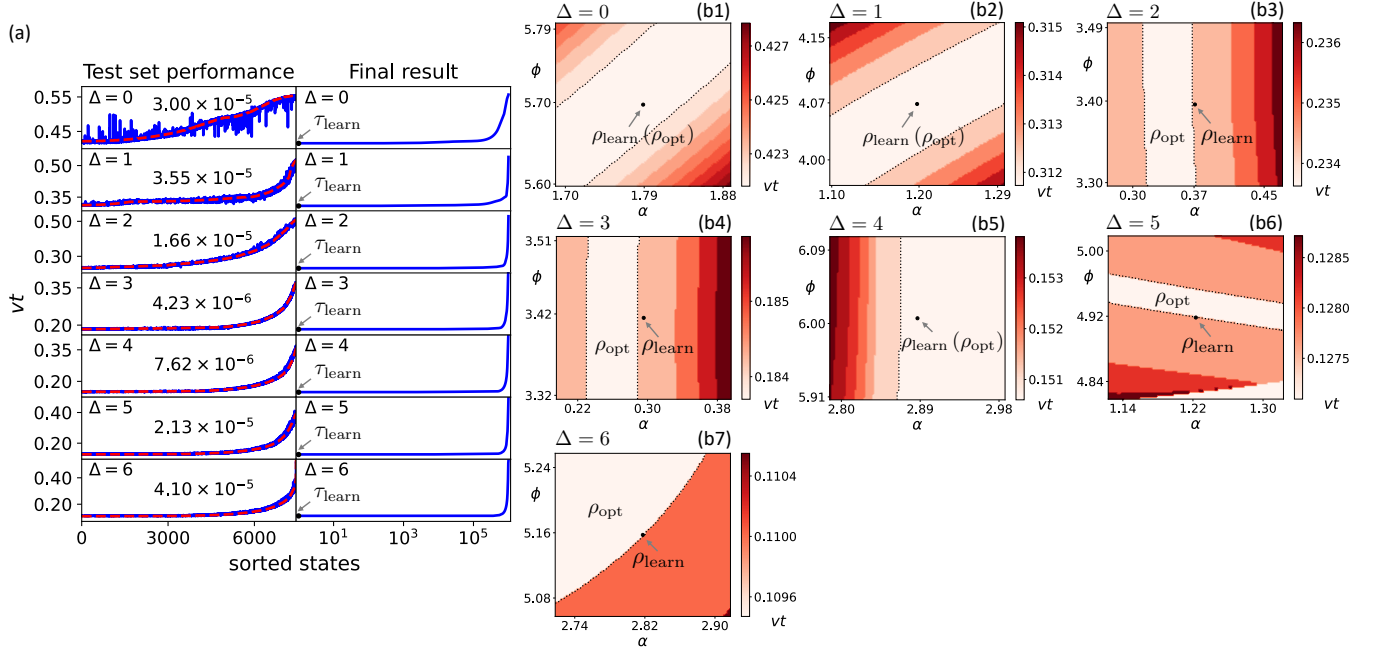


Figure 11. CRC methodology for controlled noiseless dynamics. (a) The left column: The test set performance of the regression process for  $\Delta = 0, 1, 2, 3, 4, 5, 6$  (top to bottom). The right column: The result of regression for  $\Delta = 0, 1, 2, 3, 4, 5, 6$  (top to bottom). The solid blue and dashed red lines represent the learned time and exact time obtained from regression and rigorous dynamics, respectively. The numbers in the left column are the mean square errors of learning. The  $x$  axes in both columns are in the logarithmic scales. [(b1)-(b7)] Results of calibration for  $\Delta = 0, 1, 2, 3, 4, 5, 6$ . The regime for calibration is  $[\alpha_{\text{learn}} - 0.1, \alpha_{\text{learn}} + 0.1]$  and  $[\phi_{\text{learn}} - 0.1, \phi_{\text{learn}} + 0.1]$ . The target  $\Theta$  is taken as  $\pi/2$  in all plots.

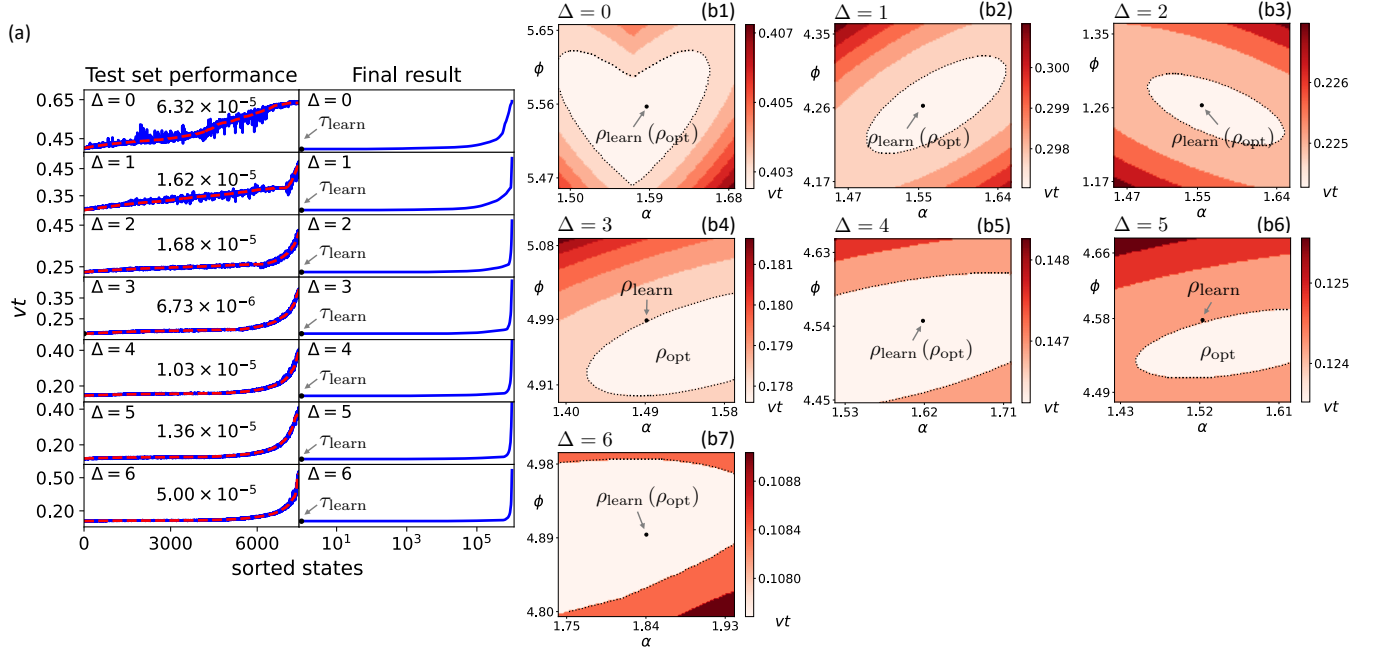


Figure 12. CRC methodology for controlled noisy dynamics. (a) The left column: The test set performance of the regression process for  $\Delta = 0, 1, 2, 3, 4, 5, 6$  (top to bottom). The right column: The result of regression for  $\Delta = 0, 1, 2, 3, 4, 5, 6$  (top to bottom). The solid blue and dashed red lines represent the learned time and exact time obtained from regression and rigorous dynamics, respectively. The numbers in the left column are the mean square errors of learning. The  $x$  axes in both columns are in the logarithmic scales. [(b1)-(b7)] Results of calibration for  $\Delta = 0, 1, 2, 3, 4, 5, 6$ . The regime for calibration is  $[\alpha_{\text{learn}} - 0.1, \alpha_{\text{learn}} + 0.1]$  and  $[\phi_{\text{learn}} - 0.1, \phi_{\text{learn}} + 0.1]$ . The target  $\Theta$  is taken as  $\pi/2$  in all plots.

and  $10^{-6}$  for all values of  $\Delta$ , as shown in the left column in Fig. 11(a). Utilizing this learned regression network, about one million states are input and corresponding learned time (solid blue lines) is given in the right column in Fig. 11(a). The minimum time  $\tau_{\text{learn}}$  for  $\Delta = 0, 1, 2, 3, 4, 5, 6$  are 0.4154, 0.3080, 0.2315, 0.1830, 0.1486, 0.1261, and 0.1113, respectively.

In the last step, the region for calibration is still taken as  $[\alpha_{\text{learn}} - 0.1, \alpha_{\text{learn}} + 0.1]$  and  $[\phi_{\text{learn}} - 0.1, \phi_{\text{learn}} + 0.1]$ . The results of calibration are given in Figs. 11(b1)-11(b7). As shown in the plots, the optimal state  $\rho_{\text{opt}}$  coincides with  $\rho_{\text{learn}}$  in the cases of  $\Delta = 0, 1, 4$ . However, the position of  $\rho_{\text{opt}}$  slightly moves away from  $\rho_{\text{learn}}$  in other cases, which proves the necessity of the step of calibration.

In the noisy case, the dephasing is invoked and the dynamics of the density matrix is governed by the master equation

$$\partial_t \rho_t = -i[H, \rho_t] + \gamma(\sigma_z \rho_t \sigma_z - \rho_t), \quad (\text{D6})$$

where the Hamiltonian is in Eq. (D2) and  $\gamma$  is the decay rate, which is taken as  $0.5\sqrt{v}$  in the following calculation. The CRC methodology has been applied in this case for  $\Delta = 0, 1, 2, 3, 4, 5, 6$  (in the units of  $\sqrt{v}$ ). The result of the classification here is the same as that in the noiseless case, i.e., all states can fulfill the target under control. The results of regression and calibration are given in Fig. 12. Similar to the noiseless case, the mean square errors of regression are still on the scales of  $10^{-5}$  and  $10^{-6}$ , as shown in Fig. 12(a). The minimum time  $\tau_{\text{learn}}$  for  $\Delta = 0, 1, 2, 3, 4, 5, 6$  are 0.3961, 0.2968, 0.2242, 0.1783, 0.1440, 0.1196, and 0.1063, respectively. In the calibration, the region for calibration is still taken as  $[\alpha_{\text{learn}} - 0.1, \alpha_{\text{learn}} + 0.1]$  and  $[\phi_{\text{learn}} - 0.1, \phi_{\text{learn}} + 0.1]$ , as shown in Figs. 12(b1)-12(b7) for different values of  $\Delta$ . The results show that  $\rho_{\text{opt}}$  are either the same with  $\rho_{\text{learn}}$ , or very close to it, indicating that both regression and calibration processes are effective in this case.

In this example, the time costs for the generation of training sets and the training of the neural networks are all less than half an hour on a regular personal computer, and that for the calibration is around 5 minutes for a value of  $\Delta$ . Hence, the CRC methodology can be easily applied to the few-body systems without any extra requirement on the computational setup.

### Appendix E: The OQSL for transverse Ising model

In this section we show the OQSL in the case of the one-dimensional transverse Ising model, of which the Hamiltonian is

$$H/J = -\sum_{j=1}^n \sigma_j^z \sigma_{j+1}^z - g(t) \sum_{j=1}^n \sigma_j^x, \quad (\text{E1})$$

where  $J$  is the interaction strength between the qubits, and  $g(t)$  is the time-dependent strength of the external field. Here we consider that  $g(t) = B \cos(\omega t)$ .

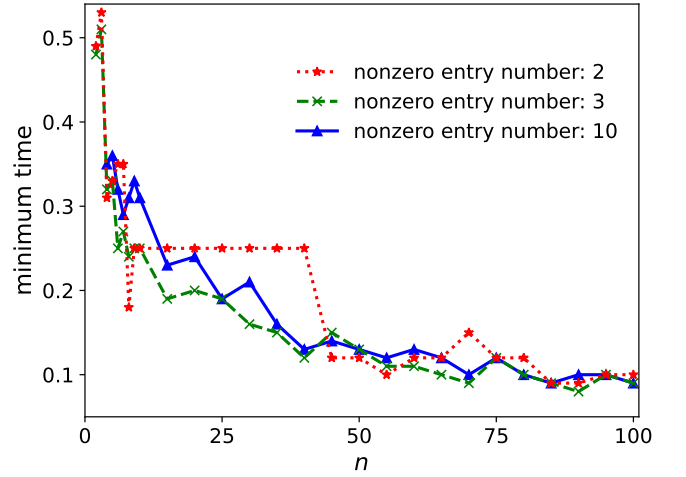


Figure 13. The minimum time to reach the target as a function of spin number  $n$  for 2000 random states with 2 nonzero entries (dotted-red-pentagram line), 3 nonzero entries (dashed-green-cross line), and 10 nonzero entries (solid-blue-triangle line). The parameters are set as  $\Theta = \pi/2$ ,  $B = 0.5$ , and  $\omega/J = 1$ .

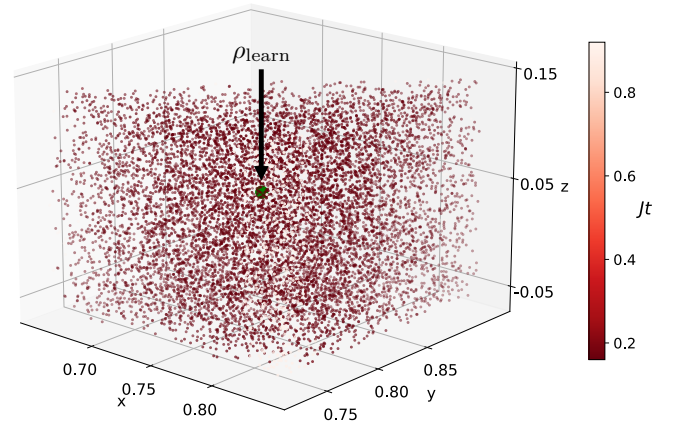


Figure 14. Calibration result in the category of states with 2 nonzero entries. The green dot is the position of  $\rho_{\text{learn}}$ .

Because of the enormous state space for this Hamiltonian, it is not easy to set up good training sets that are general enough for the CRC methodology. To feasibly apply the CRC methodology, we need to analyze the state structure first and reduce the state space for the study. A simple way to categorize the states is based on the number of nonzero entries in a certain basis. Therefore, we analyze the evolution time to reach the target for the states with different numbers of nonzero entries in the basis  $\{|\uparrow\rangle, |\downarrow\rangle\}^{\otimes n}$ . Here  $|\uparrow\rangle$  ( $|\downarrow\rangle$ ) is the eigenvalue of  $\sigma_z$  with respect to the eigenvalue 1 ( $-1$ ). The evolution time to reach the target has been calculated for 2000 random states in each category, and the minimum time is given in Fig. 13. It can be seen that the minimum time for the states with 2 (dotted-red-pentagram line) and 3 (dashed-green-cross line) nonzero entries is always lower

nonzero entry number	classification		regression			calibration
	score	ratio	mean square error	$\tau_{\text{learn}}$	true value	optimal time
2	94.55%	7.71%	$8.95 \times 10^{-4}$	0.24	0.19	0.18
3	89.67%	5.85%	$2.06 \times 10^{-2}$	0.18	0.25	0.24
4	85.44%	6.73%	$1.69 \times 10^{-2}$	0.52	0.37	0.36
5	81.52%	9.48%	$1.54 \times 10^{-2}$	0.54	0.24	0.24

Table I. Results of CRC methodology in the categories of 2, 3, 4, and 5 nonzero entries.

than that for the states with 10 (solid-blue-triangle line) nonzero entries when  $n$  is no larger than 100. This phenomenon indicates that in this example we only need to focus on the states with few nonzero entries for the study of OQSL.

In the meantime, we found an interesting phenomenon. The ratio of reachable states in the 2000 random states basically fits the function

$$\frac{1}{1 + an^b e^{-cn^d}}. \quad (\text{E2})$$

The parameters  $a, b, c, d$  are 1.132, 1.309, 0.005, 1.826 for the category of 2 nonzero entries, and 0.450, 1.654, 0.034, 1.355 for the category of 3 nonzero entries, and 0.613, 0.842, 0.007, 1.754 for the category of 10 nonzero entries. The fitting errors in three cases are 0.031, 0.028, and 0.031, respectively. For a large number of spins, basically all states can fulfill the target. We think a possible explanation for this phenomenon is that in a large Hilbert space, the number of target states for a given target is significantly large for any state, hence it is very easy to fulfill the target. The true ratio in this case and the physical mechanism behind it are still open questions and need to be further investigated in the future.

Next, we perform the CRC methodology to evaluate the OQSL. Since we only need to focus on the states with few nonzero entries, the CRC methodology is applied in the categories of states with 2, 3, 4, and 5 nonzero entries. The results are given in Table I. In all cases, 22500 and 7500 states and corresponding results (0 or 1) consist of the training and test sets in the classification process. The best score of the trained network we obtain is 94.55%, 89.67%, 85.44%, and 81.52% in the categories of 2, 3, 4, and 5 nonzero entries. The results show that 7.71%, 5.85%, 6.73%, and 9.48% states can fulfill the target in these categories. In the regression process, we also use 22500 and 7500 states and the corresponding evolution time to reach the target as the training and test sets. The best mean square errors of the trained network we obtain are  $8.95 \times 10^{-4}$ , 0.0206, 0.0169, and 0.0154 in the categories of 2, 3, 4, and 5 nonzero entries, and corresponding values of  $\tau_{\text{learn}}$  are 0.24, 0.18, 0.52, and 0.54. The true values of the evolution time of  $\rho_{\text{learn}}$  are 0.19, 0.25, 0.37, and 0.24. The gap between  $\tau_{\text{learn}}$  and the true values are majorly affected by the mean square errors, and it becomes difficult to obtain a good mean square error with the increase of the nonzero entry number. About 10000 random states in the neighborhood

of  $\rho_{\text{learn}}$  are used in the process of calibration. These states share the same positions of nonzero entries with  $\rho_{\text{learn}}$  and the differences of the norms and phases between them and  $\rho_{\text{learn}}$  are less than 0.1. The calibration in the category of 2 nonzero entries is shown in Fig. 14. The  $x$  and  $y$  axes are the norms of the nonzero entries and the  $z$  axis is the phase difference between these two entries. The green dot is the position of  $\rho_{\text{learn}}$ . The other three categories are not shown since the parameters are larger than 3. After the calibration, the optimal evolution time in these categories is 0.18, 0.24, 0.36, and 0.24. Hence, the final evaluation of OQSL in this example is 0.18, which can be realized by certain states with 2 nonzero entries.

In this example, the time cost for the generation of training sets for one category is about one day on a work station with 12 threads, and those for the training of the neural networks in the classification and regression processes are only several minutes. Moreover, the time cost of the calibration for one category is about several hours. Hence, for large-scale systems the major time cost to implement the CRC methodology is the generation of training sets.